

Research Article: New Research | Sensory and Motor Systems

Narrowly confined and glomerulus-specific onset latencies of odor-evoked calcium transients in the juxtglomerular cells of the mouse main olfactory bulb

Ryota Homma¹, Xiaohua Lv^{1,2,3}, Tokiharu Sato¹, Fumiaki Imamura⁴, Shaoqun Zeng^{2,3} and Shin Nagayama¹

¹Department of Neurobiology and Anatomy, McGovern Medical School at The University of Texas Health Science Center at Houston, Houston, TX, 77030

²Britton Chance Center for Biomedical Photonics, Wuhan National Laboratory for Optoelectronics, Huazhong University of Science and Technology, Wuhan, 430074, China

³MoE Key Laboratory for Biomedical Photonics, Collaborative Innovation Center for Biomedical Engineering, School of Engineering Sciences, Huazhong University of Science and Technology, Wuhan, 430074, China

⁴Department of Pharmacology, Pennsylvania State University College of Medicine, Hershey, PA, 17033

<https://doi.org/10.1523/ENEURO.0387-18.2019>

Received: 2 October 2018

Revised: 1 February 2019

Accepted: 5 February 2019

Published: 11 February 2019

Author contributions: R.H. and S.N. designed research; R.H., X.L., T.S., F.I., S.Z., and S.N. performed research; R.H. analyzed data; R.H. and S.N. wrote the paper.

Funding: <http://doi.org/10.13039/100000055HHS> | NIH | National Institute on Deafness and Other Communication Disorders (NIDCD) R01DC013802 R01DC016307

Funding: <http://doi.org/10.13039/501100001809National> Natural Science Foundation of China (NSFC) 81327802

The authors declare no competing financial interests.

HHS | NIH | National Institute on Deafness and Other Communication Disorders (NIDCD) [R01DC013802]; HHS | NIH | National Institute on Deafness and Other Communication Disorders (NIDCD) [R01DC016307]; National Natural Science Foundation of China (NSFC) [81327802]

RH and XL contributed equally to the work.

Correspondence should be addressed to Shin Nagayama, Shin.Nagayama@uth.tmc.edu or Ryota Homma, Ryota.Homma@uth.tmc.edu

Cite as: eNeuro 2019; 10.1523/ENEURO.0387-18.2019

Alerts: Sign up at www.eneuro.org/alerts to receive customized email alerts when the fully formatted version of this article is published.

Accepted manuscripts are peer-reviewed but have not been through the copyediting, formatting, or proofreading process.

Copyright © 2019 Homma et al.

This is an open-access article distributed under the terms of the Creative Commons Attribution 4.0 International license, which permits unrestricted use, distribution and reproduction in any medium provided that the original work is properly attributed.

1 **Title Page**

2 1. Manuscript Title (50 word maximum):

3 Narrowly confined and glomerulus-specific onset latencies of odor-evoked calcium transients in the
4 juxtglomerular cells of the mouse main olfactory bulb

5 2. Abbreviated Title (50 character maximum):

6 Odor-response properties of juxtglomerular cells

7 3. List all Author Names and Affiliations in order as they would appear in the published article:

8 Ryota Homma*¹, Xiaohua Lv*^{1,2,3}, Tokiharu Sato¹, Fumiaki Imamura⁴, Shaoqun Zeng^{2,3}, Shin
9 Nagayama¹

10 1. Department of Neurobiology and Anatomy, McGovern Medical School at The University of Texas
11 Health Science Center at Houston, Houston, TX, 77030

12 2. Britton Chance Center for Biomedical Photonics, Wuhan National Laboratory for Optoelectronics,
13 Huazhong University of Science and Technology, Wuhan, 430074, China

14 3. MoE Key Laboratory for Biomedical Photonics, Collaborative Innovation Center for Biomedical
15 Engineering, School of Engineering Sciences, Huazhong University of Science and Technology,
16 Wuhan, 430074, China

17 4. Department of Pharmacology, Pennsylvania State University College of Medicine, Hershey, PA,
18 17033

19 * RH and XL contributed equally to the work.

20 4. Author Contributions:

21 RH and SN Designed Research; RH, XL, TS, FI, SZ, and SN Performed Research; RH Analyzed
22 Data; RH and SN Wrote the paper.

23

24 5. Correspondence should be addressed to (include email address):

25 Shin Nagayama

26 P.O. Box 20708 Houston, TX 77225-0708

27 Shin.Nagayama@uth.tmc.edu

28 Ryota Homma

29 P.O. Box 20708 Houston, TX 77225-0708

30 Ryota.Homma@uth.tmc.edu

31 6. Number of Figures: 8

32 7. Number of Tables: 0

33 8. Number of Multimedia: 0

34 9. Number of words for Abstract: 240

35 10. Number of words for Significance Statement: 116

36 11. Number of words for Introduction: 663

37 12. Number of words for Discussion: 1608

38 13. Acknowledgments:

39 S.N. is supported by NIH/NIDCD Grant R01DC013802. F.I. is supported by NIH/NIDCD Grant

40 R01DC016307. S.Z. and X.L. are supported by NSFC Grant 81327802. We thank Wei R. Chen for his

41 contribution to the setup of the acousto-optic deflector two-photon microscope.

42 14. Conflict of Interest:

43 The authors declare no competing financial interests.

44 **Abstract**

45 Odor information is transmitted from olfactory sensory neurons to principal neurons at the glomeruli of
46 the olfactory bulb. The intraglomerular neuronal circuit also includes hundreds of interneurons referred to
47 as juxtglomerular (JG) cells. Stimulus selectivity is well correlated among many JG cells that are
48 associated with the same glomerulus, consistent with their highly homogeneous sensory inputs. However,
49 much less is known about the temporal aspects of their activity, including the temporal coordination of
50 their odor-evoked responses. As many JG cells within a glomerular module respond to the same stimulus,
51 the extent to which their activity is temporally aligned will affect the temporal profile of their population
52 inhibitory inputs. Using random-access high-speed two-photon microscopy, we recorded the odor-evoked
53 calcium transients of mouse JG cells and compared the onset latency and rise time among neurons
54 putatively associated with the same and different glomeruli. Whereas the overall onset latencies of odor-
55 evoked transients were distributed across a ~150 ms time window, those from cells putatively associated
56 with the same glomerulus were confined to a much narrower window of several tens of milliseconds. This
57 result suggests that onset latency primarily depends on the associated glomerulus. We also observed
58 glomerular specificity in the rise time. The glomerulus-specific temporal pattern of odor-evoked activity
59 implies that the temporal patterns of inputs from the intraglomerular circuit are unique to individual
60 glomerulus–odor pairs, which may contribute to efficient shaping of the temporal pattern of activity in the
61 principal neurons.

62

63

64 **Significance Statement**

65 The sense of smell is essential for assessing chemicals in one's atmospheric environment. In
66 understanding the biological mechanisms by which humans and animals recognize various odorous
67 chemicals, a key question is how the signals sent from the nose are transformed in the brain. In this work,
68 we studied the temporal pattern of activity in interneurons that tune the sensory inputs to the principal
69 (signal-carrying) neurons in the olfactory bulb via structures known as glomeruli. We found that the odor
70 responses of these interneurons are precisely coordinated in time, suggesting that the glomerulus is a
71 temporally well-organized unit. Our finding suggests that the temporal coordination of glomerular activity
72 is important in signal transformation in the olfactory system.

73

74

75 Introduction

76 The glomeruli in the olfactory bulb (OB) form an attractive model system for studying signal
77 processing owing to their well-documented neurons and characteristic anatomy, in which the input and
78 output pathways are well segregated. In a glomerulus, sensory inputs from olfactory sensory neurons
79 (OSNs) are transmitted to mitral/tufted cells, which in turn send the signals to higher olfactory centers.
80 Signal processing in the glomerulus involves feedforward excitation and inhibition mediated by hundreds
81 of juxtglomerular (JG) cells, the diverse interneurons (see below) located in the glomerular layer (GL)
82 (De Saint Jan et al., 2009; Najac et al., 2011; Shao et al., 2012; Carey et al., 2015; Geramita and Urban,
83 2017). One remarkable trait of these feedforward circuits is that each type of feedforward input
84 (excitatory or inhibitory) to a glomerulus is mediated by numerous JG cells of specific types. The
85 properties of collective feedforward inputs thus depend on the extent to which the activity of participating
86 neurons is temporally coordinated. However, little is known about the temporal patterns of activity among
87 JG cells that are associated with the same glomerulus.

88 The term “JG cell” is a generic name for interneurons in the GL and includes multiple types of
89 neurons: conventionally, major JG cell types include GABAergic periglomerular (PG) cells,
90 glutamatergic external tufted (ET) cells, and GABAergic/dopaminergic superficial short-axon (sSA) cells
91 (Pinching and Powell, 1971; Nagayama et al., 2014, but see Tavakoli et al., 2018). PG cells are the most
92 abundant cell type among JG cells. They are monoglomerular (their dendrites project to a single
93 glomerulus) and they receive sensory inputs directly from OSNs or disynaptically from ET cells,
94 depending on the PG cell subtype (Shao et al., 2009). ET cells are also monoglomerular and receive direct
95 input from OSNs. These two cell types are the sources of feedforward inhibition and excitation,
96 respectively, in the intraglomerular circuit through multiple subcircuits (Shao et al., 2009; Najac et al.,
97 2015). The neuronal processes of sSA cells cross multiple glomeruli and are believed to mediate
98 interactions among glomeruli within the GL (Kiyokage et al., 2010). The cellular properties and

99 connectivity of these neurons, including their subtypes, have been extensively studied (Wachowiak and
100 Shipley, 2006; Kosaka and Kosaka 2014, 2016; Burton 2017; Tavakoli et al., 2018).

101 The basic functional properties of JG cells have been revealed previously by *in vivo* recordings (Wellis
102 and Scott, 1990; Tan et al., 2010; Homma et al., 2013; Kikuta et al., 2013; Wachowiak et al., 2013;
103 Fukunaga et al., 2014; Livneh et al., 2014). For example, JG cells fire spontaneously at various rates; this
104 spontaneous activity is phasic and tuned to respiration phase in the majority of cells. In response to odors,
105 JG cell firing increases or decreases and/or shifts in phase. The relationship between glomerular inputs
106 and JG cells has been studied via electrophysiological recordings in genetically tagged glomeruli (Tan et
107 al., 2010), calcium imaging with glomerulus-specific labeling (Kikuta et al., 2013), and calcium imaging
108 with optogenetic stimulation of a genetically-targeted single glomerulus (Braubach et al., 2018). The odor
109 selectivity of JG cells is correlated with that of OSNs as well as with that of other JG cells associated with
110 the same glomerulus. However, these techniques did not allow simultaneous recording from multiple JG
111 cells at sufficient temporal resolution to analyze how the activity of these cells is temporally coordinated.
112 In this study, we used high-speed two-photon calcium recording (Grewe et al., 2010) to compare the
113 calcium transients in JG cells within and across glomeruli at a high temporal resolution. We demonstrated
114 that the time course of odor-evoked calcium transients is primarily determined by the glomerulus. The
115 onset latency of JG cells was highly heterogeneous, with a ~150 ms difference between the earliest and
116 the latest responses, but onset latency was confined to a much narrower window when we considered only
117 the cells putatively associated with the same glomerulus. Such coordinated activity in JG cells could help
118 to efficiently shape the time course of sensory inputs that are unique to the associated glomerulus.

119

120 **Materials and Methods**

121 **Materials**

122 Eight mice (one female) that were the progeny of a Gad2-IRES-Cre mouse (Taniguchi et al., 2011;
123 JAX Stock No. 10802; RRID:IMSR_JAX:010802) and a cre-recombinase-dependent tdTomato reporter
124 mouse (Ai9; Madisen et al., 2010; JAX Stock No. 7909; RRID:IMSR_JAX:007909) were used in this
125 study. An adeno-associated virus (AAV) vector that encodes the GCaMP6f gene under the synapsin
126 promoter (AAV1.Syn.GCaMP6f.WPRE.SV40) was purchased from the UPenn Vector Core. All odorants
127 were purchased from Sigma-Aldrich.

128 **Animal preparation**

129 All animal procedures were conducted in accordance with an animal protocol that was approved by the
130 Institutional Animal Care and Use Committee (IACUC) of [Author University].

131 *Viral injections.* Animals were anesthetized with an intraperitoneal injection of ketamine/xylazine
132 (10/0.5 mg/ml k/x, 12 μ l/g bodyweight). The depth of anesthesia was routinely monitored by toe pinches,
133 and additional injections of anesthetic were made to maintain the appropriate depth of anesthesia. Rectal
134 body temperature was maintained between 36.0°C and 37.0°C. The skull above the dorsal OBs was
135 exposed, and two small holes corresponding to two injection sites were made above the posterior end of
136 one OB. For each injection, a glass pipette containing the AAV suspension (no dilution: 9×10^{12} GC/ml)
137 was inserted through one of the holes. The pipette approached from the posterior side of the animal,
138 parallel to the A–P axis and tilted 30°–45° from vertical. The tip of the pipette was advanced 250–300 μ m
139 from the bulbar surface. A 320–640 nl injection was made at the rate of 64–128 nl/min with a Nanoject II
140 oil-pressure injector (Drummond) in each of the two injection sites. After surgery, mice were left to
141 recover undisturbed for 15–34 days before the recording session. With this injection protocol, uniform
142 labeling of the entire dorsal OB was observed under a fluorescence microscope. In some of the animals
143 (labeled mice 6–8 in the figures), a cranial window was implanted during the surgery for the AAV
144 injections. In these animals, a metal head-plate with a 5 mm round opening (CP-1, Narishige) was
145 attached to the skull with cyanoacrylate glue and dental acrylic. A round cranial window (~3 mm in
146 diameter) that covered both dorsal bulbs was made through the opening of the head-plate. The dura mater

147 was not removed. The exposed bulb was sealed with 0.8% agarose and a 3 mm round coverslip (CS-3R,
148 Warner Instruments), which was cemented with cyanoacrylate glue and dental acrylic.

149 *Data acquisition.* Animals previously injected with AAV were anesthetized with an intraperitoneal
150 injection of urethane (6% w/v, 20 μ l/g bodyweight for induction, with the depth of anesthesia monitored
151 by toe pinches and maintained by additional injections). Animals breathed freely throughout the
152 experiment, and rectal body temperature was maintained between 36.0°C and 37.0°C. Animals with a
153 pre-installed cranial window (see above) were transferred to the microscope stage once the level of
154 anesthesia was stable. For animals without a pre-installed cranial window, a metal head-plate was
155 attached to the skull with cyanoacrylate glue and dental acrylic. Then, a craniotomy was made in the
156 AAV-injected side of the OB and the opening was filled with 1.2% agarose and sealed with a pre-cut
157 piece of coverslip, which was cemented with cyanoacrylate glue. Following the cranial window
158 preparation, the animal was transferred to the microscope stage. The microscope stage was equipped with
159 an angle-adjustable stage (MAG-3, Narishige) to allow fine adjustments of the angle of the bulbar surface
160 relative to the objective. Breathing was monitored with a piezo-electric sensor placed beneath the chest,
161 and the signal was recorded together with the optical signals.

162 **Optical recordings**

163 All optical recordings (i.e., wide-field and two-photon) were conducted with the same upright
164 fluorescence microscope (Olympus) combined with a motorized stage (Scientifica). All optics were
165 implemented on a vibration-isolating air table (Newport). For wide-field imaging, the excitation light was
166 provided by a 470 nm LED module (M470L2, Thorlabs). The filter set was a standard GFP cube (GFP-
167 4050A-OMF-ZERO, Semrock; 466/495/525 nm exciter/DM/emitter). A 10 \times /0.3 NA objective lens
168 (Olympus) and a 0.35 \times tube lens (Olympus) were used, and the images were captured by a high-speed
169 CCD camera (NeuroCCD-SM256, RedShirtImaging) at 125 Hz for 12 s. With this configuration, a 1.75 \times
170 1.75 mm² area of bulbar surface was imaged at 128 \times 128 pixels. For two-photon recordings, a custom-
171 built acousto-optic deflector (AOD)-based two-photon scanner that is capable of random-access recording

172 was used (Iyer et al., 2006; Grewe et al., 2010). Random-access scanning is a mode of two-photon
173 recording that allows one to record from only an arbitrary set of pre-designated pixels in the field of view,
174 typically at a much higher sampling rate than conventional full-field imaging. A random-access pattern
175 scanning mode was adopted (Grewe et al., 2010), in which a fixed set of adjacent pixels were also
176 sampled in every sampling cycle so that the total light exposure time for each pixel was reduced. The
177 basic design of the AOD two-photon scanner is adopted from Lv et al. (2006). The light source was a
178 Ti:Sapphire laser (MaiTai HP DS, Spectra-Physics), and 920 nm light was used for all two-photon
179 recordings. The emitted fluorescence was routed via a dichroic mirror (FF665-Di02, Semrock) to the
180 detector module, which was located adjacent to the filter cube to minimize the length of the light path.
181 The detector module contained an IR-block filter (FF01-680/SP, Semrock) as well as a 562 nm dichroic
182 mirror (FF562-Di02, Semrock) that separates shorter (green) and longer (red) wavelength light. The
183 separated shorter and longer wavelengths of light were detected by a GaAsP photosensor module
184 (H7422A-40, Hamamatsu) and a photomultiplier tube (R1924A, Hamamatsu), respectively. Full-frame
185 scan recordings for functional imaging were made at 2.1 Hz for 15 s with a resolution of 217×217 pixels.
186 With the Olympus $25\times/1.05$ NA objective lens that used in this study, the field of view was 219×219
187 μm^2 . For the high-speed random-access recordings, 15 sites were pre-determined on the basis of the odor-
188 response data obtained during the frame scan recordings (Fig. 2B; see also Figs. 3B, 4B). Due to
189 relatively low fluorescence intensity of GCaMP6f in the pre-stimulus period, some of the cells were
190 identifiable only during odor-evoked responses. Although the system is capable of recording a larger
191 number of sites (at a lower sampling rate), 15 was about the maximum number of cells with clear odor-
192 evoked responses that could be identified from a given field of view. Therefore, all random-access
193 recordings presented in this study were conducted with 15 sites, each of which covered a single neuron, at
194 a sampling rate of 667 Hz for 15 s.

195 **Stimulus presentation**

196 Odor stimuli were presented via a custom-built olfactometer. Briefly, a mixture of odorous gas (diluted
197 odorant bubbled with 100% nitrogen) at 100 ml/min and carrier gas (filtered air) at 400 ml/min was
198 continuously supplied but continuously vacuumed near the tip of the applicator. The vacuum was
199 suspended with an electric command signal, resulting in the presentation of odorous gas until the vacuum
200 resumed. In a test conducted with a photo-ionic odorant sensor (mini PID model 200B, Aurora Scientific),
201 the onset and offset of actual odorant delivery was delayed by approximately 100 ms relative to the
202 timing of the command signals. The olfactometer was controlled by a custom-written program in
203 LabVIEW (National Instruments; RRID:SCR_014325) that enabled the stimulus presentation to be
204 synchronized to the respiration cycle of the mouse. Four seconds after the onset of data acquisition, the
205 command signal for an odor stimulus was sent at the peak of the first respiration signal (corresponding to
206 the end of an inhalation cycle) so that the odorant did not reach the mouse in the middle of an inhalation.
207 The duration of the stimulus was either 2 s or a single respiration cycle, in which case the command
208 signal to terminate the odor stimulus was sent at the peak of the respiration signal in the immediately
209 subsequent cycle.

210 For the odor stimuli, five single-molecule odorants that were aliphatic aldehydes with carbon chain
211 lengths of three to seven (referred to as 3–7CHO, respectively) were used. All odorants were diluted
212 1:100 with mineral oil and further flow-diluted 1:5 at the olfactometer. Therefore, the nominal final
213 concentration of the odorants was 0.2%. Five odorants (3–7CHO) were presented in a block design, with
214 each odorant presented once in a block of five trials. For mice 1–5, the odorant presentation order was the
215 same in every block. For mice 6–8, the order was pseudo-randomized with the constraint that the same
216 odorant was not presented in two sequential trials. In alternate blocks, the stimulus was presented for 2 s
217 or for a single respiration cycle.

218 **Immunohistochemistry**

219 Mice were deeply anesthetized and fixed by transcardial perfusion with 4% paraformaldehyde in 0.1 M
220 sodium phosphate buffer (pH 7.4). Then, brain samples were collected and post-fixed overnight at 4°C.

221 The samples were cryoprotected in 30% sucrose (w/v) in PBS (pH 7.4) and embedded in optimal cutting
222 temperature compound (Sakura Finteck). The olfactory tissues were cut on a cryostat into 20 μm sections
223 (coronal) and stored at -20°C until use. The slices were pretreated in TBS-T (10 mM Tris-HCl (pH 7.4),
224 100 mM NaCl with 0.3% Triton-X100 (v/v)) for 15 min and blocked with blocking buffer (5% normal
225 donkey serum (v/v) in TBS-T) at $20-25^{\circ}\text{C}$ for 1 h. The slices were then incubated with primary
226 antibodies diluted in blocking buffer overnight at 4°C . Sections were washed with TBS-T, then incubated
227 with secondary antibodies for 1 h. The immunoreacted sections were washed and mounted with
228 FLUORO-GEL mounting medium (Electron Microscopy Sciences, #17985-11).

229 The following antibodies were used. Primary antibodies: anti-GABA (MilliporeSigma, #A2052, rabbit,
230 1:100) and anti-TH (MilliporeSigma, #AB152, rabbit, 1:500). Secondary antibody: Alexa Fluor 488
231 donkey anti-rabbit IgG (Thermo Fisher Scientific, #A21206, 1:300).

232 Six to eight serial images were captured at intervals of 1.5 μm with an Olympus FluoView FV1000
233 laser scanning confocal microscope with a $20\times$ objective lens (UPLSAPO $20\times$), with or without $4\times$
234 digital zoom. Then, the acquired images were converted to a Z-stack with the software FV10-ASW
235 viewer (Olympus).

236 **Data analysis**

237 There were minor differences in the experimental conditions (e.g., the timing of the craniotomy and
238 the order of stimulus presentation; see above) between the two subsets of mice (mice 1–5 versus mice 6–
239 8). Since no difference was noticed between the data from these two subsets, they were not discriminated
240 in any of the following analyses. All data analyses and preparation of figures were carried out in
241 Fiji/ImageJ (Schindelin et al., 2012; RRID:SCR_002285) and MATLAB (MathWorks,
242 RRID:SCR_001622) with custom scripts. In the recordings in this study, photobleaching of fluorescence
243 within a trial was negligibly small compared to the evoked responses with which the onset latency and
244 rise time were analyzed. However, during the process of grouping cells based on the stimulus selectivity

245 (see below), photobleaching was not negligible for the subset of trials that showed little or no odor-
246 evoked response. (Such trials were not included in the subsequent analyses.) Therefore, the
247 photobleaching was corrected for during the process of grouping, but the uncorrected data were used in
248 the rest of analyses because no considerable benefit of correction were recognized.

249 *Spatiotemporal activity maps.* For wide-field imaging, spatial patterns of odor-evoked activity were
250 visualized as the difference between images from the pre-stimulus period and the response period (i.e.,
251 $\Delta F/F_0$ maps; Fig. 2A). A baseline image from the pre-stimulus period was obtained by averaging the
252 frames from 3 to 4 s after acquisition onset. Images for three different response periods (early, middle,
253 and late) were obtained by averaging the frames in the 2 s time windows following 4.5, 6.5, or 8.5 s,
254 respectively, from the acquisition onset (0.5, 2.5, 4.5 s from the stimulus onset). In this specific analysis,
255 the trial-by-trial jitter of inhalation onset or stimulus onset was not taken into account. Then, the pre-
256 stimulus-period image was subtracted from each of three response-period images. The subtracted images
257 were divided by a spatially filtered pre-stimulus-period image (two passes of a 3×3 mean filter) for
258 normalization. After the division, the resulting image was also filtered by two passes of a 3×3 mean
259 filter. Red, green, and blue color channels were assigned to the resulting images for the early, middle, and
260 late response periods, respectively, and then all three channels were merged to form a full-color map.
261 Therefore, the brightness of the resulting activity maps reflects the response amplitude and the hue
262 reflects the character of the response time course. The intensity scale was set to the same value in each of
263 the three color channels. Essentially the same procedure was applied to obtain the activity maps for two-
264 photon full-frame imaging (Fig. 2B).

265 *Basic signal processing of the time-course data.* Data from two-photon random-access recordings are not
266 a series of images, but a set of time series that resemble the data from multi-electrode recordings. Thus,
267 no image processing is involved in the analysis. Time courses were converted to $\Delta F/F_0$ by subtracting the
268 averaged data from the first 1% of data points (150 ms; F_0) and then dividing by F_0 . A box filter with a
269 100 ms window was applied to all the time courses unless specified.

270 *Response-based grouping of cells.* The subset of recorded cells that surrounded the same glomerulus had
271 highly correlated odor selectivity (Figure 3). Under the assumption that these neurons were associated
272 with the same glomerulus, such neurons were grouped using the following two criteria. First, each
273 neurons was directly facing the glomerulus of interest so that no other glomerulus was located between
274 the cell and the glomerulus. When a cell was directly facing more than one glomerulus, all of the facing
275 glomeruli were considered for the second criterion with the other neurons surrounding each glomerulus.
276 Second, the response profile of a given neuron was closer to that of all the in-group recorded neurons than
277 to that of any out-group recorded neurons. In other words, the least similar in-group neuron had a more-
278 similar response profile than the most-similar out-group neuron. Comparisons of similarity were made
279 simultaneously but not in an agglomerative manner. When a subset of the cells that meet the first criterion
280 did not meet the second, those cells were removed from the group. Cosine similarity (cosine of the angle
281 between two vectors) was used as a measure of the similarity between two response profiles. A response
282 profile here is defined as a vector representing the response amplitudes to the five different odors, or a
283 vector representing all pairwise differences (ten pairs from five odorants) of response amplitudes. When
284 at least one of these two response profiles satisfied the above criteria, the neuron was considered as
285 qualified. Response amplitudes were defined as the integral of the $\Delta F/F_0$ trace (area under the trace) from
286 the trials with single-respiration-cycle stimulation. In this analysis, since even tiny responses are
287 potentially influential, photobleaching/drift was corrected for by subtracting a straight line that was best
288 fitted to the 0–4 s (pre-stimulus period) and the 14–14.5 s period (post-response period) of the time course,
289 only when the average of the latter period had a negative value. The correction was made only in the trials
290 with downward changes because (1) prominent photobleaching/drift was observed only in the negative
291 direction, and (2) applying correction to positive values would significantly distort the subset of data that
292 showed long-lasting odor responses.

293 *Determining the onset latency and rise time of calcium transients.* The onset latency of an odor-evoked
294 calcium transient was defined via the following procedure (see also a visual explanation in Fig. 5A). All

295 $\Delta F/F_0$ traces were preprocessed with a 50 ms box filter. For a given trace, the baseline period was defined
296 as a 100 ms time window immediately before the stimulus onset (the onset of the command signal). The
297 baseline $\Delta F/F_0$ level was determined as the mean value over the baseline period. To determine the noise
298 level, the 4 s pre-stimulus period was divided into eight 0.5 s blocks, calculated the standard deviation
299 within each block, and then selected the minimum among these. This procedure effectively eliminated the
300 contribution of the occasional calcium transient (see Fig. 4A) on the noise level. The provisional onset
301 latency was determined as the first time point in which 95% of the data points in the subsequent 100 ms
302 exceeded the threshold (2.5 times the noise level). Then, the trace within the subsequent 100 ms time
303 window was fitted to a straight line. The intersection of the fitted line and the baseline level was
304 considered the onset of the calcium transient. The onset latency was defined as the duration from the
305 onset of the first inhalation with the odor stimulus to the onset of the calcium transient. Although this
306 procedure determined the onset time more accurately than simple threshold methods in high signal-to-
307 noise (s/n) ratio data, it frequently resulted in obviously wrong values when the s/n ratio was lower.
308 Therefore, for this analysis, only data with a relatively high s/n ratio were considered. The s/n ratio was
309 determined as the slope of the fitted line (in $\Delta F/F_0$ per s) divided by the noise level defined above (in
310 $\Delta F/F_0$). The threshold s/n ratio was determined empirically and set to 40 (s^{-1}). In addition, in a small
311 fraction of trials, the onset of odor-evoked calcium transients accidentally coincided with a “spontaneous”
312 calcium transient. Such trials were discarded. The estimated onset latency was used for further analysis
313 (presented in Figs. 5–7) when the latency was successfully estimated in three or more trials (out of 5–17
314 trials) for a given cell–odor pair.

315 The rise time of an odor-evoked transient was defined as the duration between the time points when
316 the signal reached 20% and 80% of the peak amplitude. For this analysis, all $\Delta F/F_0$ traces were
317 preprocessed with a 100 ms box filter. The baseline level was defined in the same way as the protocol for
318 determining onset latency (see above). The peak amplitude was determined as the maximum value of the
319 moving average of a 100 ms time window. Time points at 20% and 80% of the peak amplitude were

320 defined as the earliest time point when half of the data points exceeded the threshold value in a 100 ms
321 time window centered at the time point being considered.

322 To compare the onset latency and rise time between tdTomato⁺ and tdTomato⁻ neurons, taking into
323 account their glomerular association, relative onset latency and relative rise time were used. Relative
324 latency, for example, was defined for each group of cells putatively associated with the same glomerulus
325 (including both tdTomato⁺ and tdTomato⁻ neurons). Subset of groups did not include any tdTomato⁻
326 neurons and thus were excluded from the analysis. The relative latency ranged from zero (shortest) to one
327 (longest), with equal spacing among neurons in the same group. For instance, if a group contained five
328 neurons, their relative latencies would be 0, 0.25, 0.5, 0.75, and 1, from shortest to longest onset latency.
329 If tdTomato⁺ neurons have shorter or longer onset latencies on average, the distribution of relative onset
330 latencies would be different in tdTomato⁺ and tdTomato⁻ neurons. The same method was applied to rise
331 times.

332 **Experiment design and statistical analyses**

333 Eight Gad2-tdTomato mice were used (seven males and one female (mouse 2); 12–32 weeks old at the
334 time of recording). Imaging experiments were carried out in one bulb from each animal. The glomerulus-
335 level analysis of onset latency (Fig. 6) includes data from 12 glomeruli in 7 mice. The glomerulus-level
336 analysis of rise time (Fig. 8) includes data from 10 glomeruli in 6 mice. The comparisons between
337 tdTomato⁺ and tdTomato⁻ neurons (Figs. 6 and 8B) were carried out on fewer cells and glomeruli, those
338 that satisfied additional criteria (see Results).

339 Normality of the data is not assumed in the statistical tests. P-values less than 0.05 were considered
340 statistically significant. The following is a list of the statistical tests used. Fig. 4D: Mann-Whitney U-test.
341 Fig. 5B: Kruskal-Wallis test, for comparisons among cell–odor pairs. Fig. 6: Kruskal-Wallis test, for
342 differences across glomerulus–odor pairs (in median onset latencies and in single trial onset latencies);
343 Mann-Whitney U-test for the comparison of glomerulus-controlled relative onset latency (see the

344 previous section) between tdTomato⁺ and tdTomato⁻ neurons. Fig. 7C: Wilcoxon signed-rank test. Fig.
345 8B Kruskal-Wallis test, for differences across glomerulus-odor pairs. Mann-Whitney U-test for the
346 comparison of glomerulus-controlled relative rise time between tdTomato⁺ and tdTomato⁻ neurons. Fig.
347 8C Mann-Whitney U-test for the comparison of relative onset latencies (in logarithm) between the
348 different subsets of data (see figure legend to Fig. 8C for detail) with no correction for multiple
349 comparisons.

350

351 **Results**

352 To analyze temporal coordination among JG cells in the glomerular network, we paid special attention
353 on PG cells. PG cells are monoglomerular and are thus thought to receive little or no direct input from
354 other glomeruli (Wachowiak and Shipley, 2006; Kiyokage et al., 2010). In addition, they are the most
355 abundant cell type in the GL and can be genetically labeled. We thus thought that PG cells would be an
356 excellent reference population in the analysis of possible functional heterogeneity among JG cells. Rather
357 than selectively expressing the genetically encoded calcium indicator (GECI) GCaMP6f in PG cells, we
358 genetically labeled PG cells with a red-fluorescent protein tdTomato and expressed GCaMP6f via an
359 injected AAV vector under the pan-neuronal synapsin promoter. This labeling strategy allowed us to
360 record from genetically identified PG cells as well as neighboring neurons of other types.

361 **Expression pattern of fluorescent proteins**

362 We used GAD2 (GAD65) as a molecular marker for a subset of PG cells (Kiyokage et al., 2010) in the
363 GL, and genetically labeled this subset with a cre-dependent tdTomato reporter mouse (Madisen et al.,
364 2010) that was crossed with a Gad2-IRES-Cre mouse (Taniguchi et al., 2011). First, we examined the
365 expression pattern of tdTomato (Fig. 1). tdTomato expression was observed in the GL and all inner layers
366 of the OB. We occasionally observed off-target tdTomato expression in a small subset of OSN axon
367 bundles as well (data not shown). In the GL, while many JG-cell somata were labeled with tdTomato,

368 fluorescence in the glomeruli was less prominent. Nearly all tdTomato⁺ somata were also positive for
369 GABA immunolabeling (Fig. 1A). A previous study reported that ~37% of JG cells were positive for
370 GAD65, ~32% were positive for GAD67, and ~16% were positive for both GAD67 and GAD65 (Parrish-
371 Aungst et al., 2007). Therefore, we expected to observe a significant proportion of GABA⁺/tdTomato⁻
372 cells, corresponding to GAD67⁺/GAD65⁻ cells, but this was not the case. We speculate that some of the
373 GAD67⁺/GAD65⁻ cells may have expressed Cre-recombinase (under the Gad2 promoter) earlier in the
374 animal's life and thus expressed tdTomato. In this scenario, tdTomato⁺ neurons would represent both
375 GAD65⁺ JG cells and a subset of GAD67⁺/GAD65⁻ cells. This raises the possibility that sSA cells, a
376 separate class of JG cells positive for GAD67 (Kiyokage et al., 2010), were included in the tdTomato⁺
377 cells. Therefore, we next examined the co-expression of tdTomato and tyrosine hydroxylase (TH), which
378 is a marker of sSA cells in the OB (Kiyokage et al., 2010; Banerjee et al., 2015) (Fig. 1B). We found that
379 TH⁺ cells included both tdTomato⁺ and tdTomato⁻ subpopulations (see white and yellow arrowheads in
380 Fig. 1B). This result is qualitatively consistent with the report that a subpopulation of TH⁺ JG cells
381 expresses GAD65 (Parrish-Aungst et al., 2007). In a previous study (Wachowiak et al., 2013), TH
382 expression in JG cells was compared with GCaMP3 expression driven by the same mechanism as
383 tdTomato in this study (a cre-dependent GCaMP3 reporter mouse crossed with the same Gad2-IRES-Cre
384 driver mouse). They reported that 14% of TH⁺ cells co-expressed GCaMP3, whereas the proportion of
385 TH⁺/tdTomato⁺ cells among TH⁺ cells in this study appears higher, for unknown reasons. To summarize,
386 tdTomato expression was specific to GABAergic neurons but may not be restricted to GAD65⁺ neurons;
387 thus we cannot rule out the possibility that a small proportion of tdTomato⁺ cells might represent sSA
388 cells. Because we did not find conclusive difference between tdTomato⁺ and tdTomato⁻ cells in the
389 following analyses, we did not further characterize the identity of tdTomato⁺ cells.

390 **Odor-evoked calcium transients in GCaMP-labeled glomeruli**

391 At the beginning of the recording session for each mouse, we checked the positions of glomeruli that
392 were responsive to our stimulus set by recording the odor-evoked response in a large portion of the dorsal

393 bulb with a high-speed CCD camera (Fig. 2A). Each panel in Fig. 2A2–4 is a combination of three
394 activity maps that represent three different time windows (see Materials and Methods for detail). The
395 early response (0.5–2.5 s after stimulus onset) is presented in red, the responses in subsequent time
396 windows (2.5–4.5 and 4.5–6.5 s) are presented in green and blue, respectively, and the three maps are
397 color-merged to produce the final image. Therefore, reddish colors imply dominance of the early response
398 and whitish colors imply long-lasting responses, for example. Consistent with previous reports (Mori et
399 al., 2006), strong activity was elicited by aliphatic aldehydes with different carbon chains. The central
400 region of the dorsal OB in Fig. 2A shows many globular and spatially distinct centers of activity, which
401 each primarily represent the activity of an individual glomerulus. These glomeruli show relatively
402 prolonged activity even after the odor stimulation (white or yellow regions). By contrast, the lateral side
403 of the bulb (top of the images) shows activity that declines quickly after stimulus offset (red regions).
404 There are also glomeruli that appear bluish in color (see Fig. 2A3), which represents a slow-rising
405 calcium signal that peaked long after the stimulus offset. It is apparent that the time courses of odor-
406 evoked calcium transients are diverse and depend on the particular glomerulus–odor pair. Of note,
407 multiple cell types contributed to these signals from wide-field imaging because GCaMP6f was expressed
408 under the control of the synapsin promoter. Therefore, the signals reflect not only the glomerular activity
409 but also the activity of somata and other neuronal processes, including the inter-glomerular processes of
410 sSA cells (Kiyokage et al., 2010) and processes in the inner layers.

411 **Odor-evoked calcium transients in GCaMP-labeled JG cells**

412 For two-photon recordings of individual JG cells, we chose the recording location guided by the data
413 from wide-field imaging. Briefly, we first identified a candidate location where we found a cluster of
414 several glomeruli, each of which responded to our stimulus set with a discriminable odor selectivity. At
415 the location, we first conducted conventional XYT scans to assess the odor-evoked response of glomeruli
416 and JG cells (Fig. 2B). On the basis of the shape and “color” of the activity maps, we could reliably match
417 the glomeruli in the two-photon imaging with those in the wide-field imaging (Fig. 2). We kept the

418 recording depth relatively shallow (45–98 μm , $62.8 \pm 16.6 \mu\text{m}$ mean \pm sd, from the dura mater) so that the
419 glomeruli were included in the field of view. Since we needed to determine the recording sites (regions of
420 interest; ROIs) for random-access scanning prior to the recording, we next picked 15 cells on the basis of
421 the two-photon response maps (e.g., Fig. 2B) and the two-photon microscope images including those
422 during odor-evoked responses (e.g., Figs. 3B, 4B; see also the Materials and Methods). Among 120 cells
423 from 8 recordings, 79 cells (66%) were identified as tdTomato⁺ (9.9 ± 2.6 per recording, mean \pm sd). The
424 tdTomato⁻ recorded cells may include GAD65⁻ PG cells, sSA cells, and ET cells. ET cells, however, may
425 be under-represented, considering that the AAV vector we used (AAV2/1) preferentially infects PG
426 and/or sSA cells (Adam et al., 2014) and that the somata of ET cells are located in the deeper part of the
427 GL (Pinching and Powell, 1971; Macrides and Schneider, 1982; Hayar et al., 2004). As both GCaMP6f
428 and tdTomato labeling were relatively dense, we had little morphological information of the individual
429 recorded cells such as whether the dendrites were monoglomerular or multiglomerular.

430 Examples of odor-evoked calcium transients are presented in Fig. 3A. Because the random-access
431 recording method records data only from a set of pre-determined ROIs (see Figs. 3B and 4B), the
432 obtained data is not a series of XY images but multiple traces from the ROIs (optical multi-ROI
433 recording). Conventionally, odor-evoked responses are measured by presenting odors for several seconds
434 (2 s in this study) as shown in Fig. 3A (left panel). The responses to a 2 s stimulus exhibited some
435 diversity in their time courses. Whereas previous electrophysiological experiments demonstrated that
436 odor-evoked responses of PG cells tend to occur as bursts of action potentials that are locked to the
437 respiration cycle (Tan et al., 2010; Homma et al., 2013; Livneh et al., 2014), we observed respiration-
438 locked modulation of calcium signals in only a minor subset of traces (Fig. 4A). In the neurons of mouse
439 visual cortex, GCaMP6f was capable of resolving two spikes with an interval of 50–75 ms as a stepwise
440 increase of calcium signal or those with an interval of >100 ms more clearly (Chen et al., 2013). As the
441 duration of a respiration cycle in this study ranged 300–500 ms (120–200 cycle/min), the intervals
442 between the bursts might be marginal for being resolved clearly when the respiration was relatively high

443 and the bursts themselves also occupy a significant portion of the cycle. The typical time course of the
444 odor-evoked calcium transients with 2 s stimulation was a monotonic rise followed by a monotonic
445 decline, at various rates for each (Fig. 3A). However, the number of respiration cycles for the transients to
446 reach the peak was heterogeneous. In some cases, the signal reached its peak amplitude during the first
447 odor inhalation, while in other cases it took two or more inhalations to reach the peak. Although such
448 heterogeneity in the response time course of JG cells is consistent with that observed in previous calcium-
449 imaging studies (Wachowiak et al., 2013; Adam et al., 2014), this heterogeneity complicates the
450 physiological implications of information extracted from the calcium signal (e.g., the peak amplitude). To
451 obtain simpler and more comprehensible time courses, we used briefer stimuli that were controlled to the
452 duration of a single respiration cycle (see Materials and Methods). The right panel of Fig. 3A shows
453 examples of responses to such single-cycle stimuli. As expected, we observed more-stereotyped time
454 courses with these stimuli than with multi-cycle (2 s) stimuli.

455 **Response-based estimation of associated glomerulus**

456 JG cells that are associated with the same glomerulus show highly correlated stimulus selectivity (Tan
457 et al., 2010; Kikuta et al., 2013) likely because they receive most of inputs from the glomerulus, and are
458 thought to be located in the proximity of the associated glomerulus (Homma et al., 2013; Kikuta et al.,
459 2013; Adam et al., 2014; Braubach et al., 2018). We thus reasoned that we could infer the association
460 between the recorded cells and a particular glomerulus from their odor response and the location of the
461 cell body. By comparing the odor-evoked responses to different odors, we observed that some of the
462 recorded cells indeed showed highly correlated response profiles including odor selectivity (Fig. 3C). To
463 systematically compare the odor responses, we used the data from single-cycle stimulation trials and
464 calculated the response amplitude, defined as the integral of each $\Delta F/F_0$ trace (i.e., the area under the
465 trace). The five-element response vectors (middle panel of Fig. 3C) that represent the response amplitudes
466 to the five odors were often sufficient for comparison. However, we also considered the ten-element
467 difference vectors that were composed of the differences between every pair of response amplitudes (right

468 panel of Fig. 3C); these were useful to distinguish between the subsets of cells with relatively similar
469 response vectors. Combining these data with the location of individual cells (Fig. 3B), we grouped
470 together the cells that surrounded the same glomerulus and that showed highly correlated odor selectivity,
471 and assumed that these neurons were associated with the same glomerulus (Fig. 3B2, C; see Materials and
472 Methods for details). Note that only odor selectivity that was based on the time-averaged data (area under
473 the trace) were used for this glomerulus-assignment process (in addition to the location of cell body). We
474 deliberately avoided employing the temporal patterns of calcium transients during this process because
475 we will discuss the dynamics of calcium transients with reference to these groups in the subsequent
476 analyses. In the representative case shown in Fig. 3, we identified two groups of four cells each (shown in
477 red and blue). We also found another group with two cells (shown in brown), although this group was not
478 considered in the subsequent analyses because it contained too few cells. We were able to find 14 groups
479 of three or more cells that satisfied the criteria in the eight fields of view from eight mice.

480 **Baseline activity of the GCaMP-labeled JG cells**

481 Prior to a detailed analysis of the odor-evoked response, we briefly characterized the calcium signals
482 in the pre-stimulus period and examined if they could potentially affect the analyses of the odor-evoked
483 responses (Fig. 4). Fig. 4A represents examples of traces during the pre-stimulus period. Whereas
484 previous electrophysiological recordings reported that some JG cells exhibit action potentials that are
485 coupled to the respiration cycle even without an odor stimulus (Homma et al., 2013, Livneh et al., 2014;
486 Najac et al., 2015), we did not observe calcium signals that were regularly coupled to the respiration cycle
487 in our cellular recordings despite a sufficiently high sampling rate. Possible explanations may include
488 relatively few action potentials per cycle, relatively slow kinetics of either the GECI signal or intracellular
489 calcium itself in the cell body, which may mask the respiration-locked modulation, or a combination of
490 these. Alternatively, it may be also possible that we failed to reliably detect the individual cycle of stable
491 respiration-locked bursts within the persistently elevated intracellular calcium that is caused by the burst
492 themselves (Homma et al., 2013). In contrast to the (apparent) lack of respiration cycle-locked transients,

493 we observed occasional fluctuations of the GCaMP signal that were absent or much less prominent in the
494 simultaneously recorded red fluorescence from calcium-insensitive tdTomato. To compare the size of pre-
495 stimulus fluctuations with the size of the odor-evoked response, we calculated the ratio of the peak
496 amplitude of the odor-evoked response to the range (the difference between the 1st and 99th percentiles)
497 of the pre-stimulus period signal (Fig. 4C). In the vast majority of cell–odor pairs ($s/n > 1$ in 99.7% of the
498 cell–odor pairs with odor-evoked responses), the odor-evoked response was much larger than the pre-
499 stimulus fluctuation, suggesting that the pre-stimulus activity would not significantly affect the analysis
500 of odor-evoked calcium transients that we discuss in the following sections.

501 We also noticed that signal fluctuations during the pre-stimulus period tend to be synchronized among
502 the cells putatively associated with the same glomerulus (see previous section). This observation suggests
503 that pre-stimulus activity is driven by some form of glomerular input or spontaneous local network
504 activity within a glomerulus. To examine this possibility, we calculated the pairwise Pearson’s correlation
505 coefficient between the time courses during the pre-stimulus period for all simultaneously recorded pairs
506 of cells. The distribution of correlation coefficients is presented separately for the cells putatively from
507 the same glomerulus and all other pairs (Fig. 4D). The correlation coefficients were significantly higher in
508 the “same glomerulus” pairs than in the “all others” pairs ($P = 2.4 \times 10^{-25}$, Mann-Whitney U-test for the
509 same distribution, $N = 135$ and 705 pairs of cell–odor pairs for the “same glomerulus” and “all others”
510 groups, respectively). This result suggests some degree of synchrony in the pre-stimulus activity among
511 the JG cells associated with the same glomerulus. There is a chance that the “all others” pairs may include
512 some in which both cells were actually associated with the same glomerulus but that were mislabeled
513 owing to our relatively conservative procedure for cell grouping.

514 **Glomerulus-specific onset latencies of odor-evoked calcium transients**

515 The somatic calcium transients primarily reflect the action potentials of the cell (Chen et al., 2013,
516 Homma et al, 2013). Although it is difficult to infer the precise time course of bursts of action potentials
517 from an odor-evoked calcium transient, it is more feasible to determine the onset latency of the transient,

518 which reflects the onset of the burst. Therefore, we analyzed the onset latency of odor-evoked calcium
519 (Figs. 5–7). First, we carefully determined the onset latency from our high-sampling-rate data (Fig. 5A;
520 see Materials and Methods for details). Briefly, we approximate the earliest part of the rising signal as a
521 linear line; the time of onset is defined as the time when this line intersects the baseline. The onset latency
522 was defined as the difference between the time of onset and the onset of inhalation estimated from the
523 respiration signal. Fig. 5B presents onset latencies from cell–odor pairs in which onset latencies were
524 successfully determined in at least five trials. Although the trial-by-trial deviation was relatively large, as
525 shown by the IQR in Fig. 5B, the median onset latency was not the same across cell–odor pairs ($P = 1.8 \times$
526 10^{-144} , $N = 165$ cell–odor pairs: Kruskal-Wallis test for non-uniform distribution). The median onset
527 latencies of tdTomato⁺ and tdTomato⁻ cells were largely overlapping, with a trend that cell–odor pairs
528 from tdTomato⁺ cells had shorter onset latencies (Fig. 5C). In a simple statistical analysis in which all
529 data points were treated as independent, this difference was statistically significant ($P = 0.011$, Mann-
530 Whitney U-test; tdTomato⁺: median 84 ms, IQR 59 ms, 105 cell–odor pairs; tdTomato⁻: median 108 ms,
531 IQR 47 ms, 60 cell–odor pairs). The distribution of onset latencies ranged from 0 to 150 ms. Although we
532 do not know precisely why the shortest onset latencies were so close to the onset of inhalation (0 ms), our
533 speculation is that the respiration signals recorded from chest movements may lag behind the inhalation at
534 the nose (Grimaud and Murthy, 2018). If this is indeed the case, then every onset latency reported in this
535 study is underestimated by a certain amount.

536 The causes of heterogeneity in onset latency may include (1) heterogeneous inputs to different
537 glomeruli, (2) differential interactions with the glomerular circuits, or (3) differences in cell type. Since
538 the majority of our recorded cells were PG cells, differences in cell type are unlikely to explain all of the
539 heterogeneity. If heterogeneous inputs to different glomeruli are the primary cause, the deviation in onset
540 latency should be much smaller among the JG cells associated with the same glomerulus. Therefore, we
541 examined onset latencies in the groups of cell–odor pairs putatively associated with the same glomerulus
542 to compare the onset latencies within and across glomeruli (Fig. 6). The median onset latencies of cell–

543 odor pairs putatively associated with the same glomerulus were distributed in relatively narrow time
544 windows compared with the distribution as a whole, suggesting that onset latency is primarily dependent
545 on the glomerulus ($P = 2.9 \times 10^{-9}$, 88 median onset latencies from 20 glomerulus–odor pairs, Kruskal-
546 Wallis test for non-uniform distribution; also see Fig. 7C). Considering the relatively large IQRs across
547 repetitions in each cell–odor pairs, we also applied the same statistical test for the onset latencies from
548 individual trials (pooled over all cells in the given glomerulus–odor pair) against glomerulus–odor pair,
549 and obtained a consistent result ($P = 3.5 \times 10^{-109}$, 1003 single trial onset latencies from 20 glomerulus–
550 odor pairs, Kruskal-Wallis test). Importantly, there were cases in which different odors resulted in
551 discriminable onset latencies for cells within the same glomerulus (e.g., mouse 2 and mouse 4 in Fig. 6),
552 implying that the onset latency depends on both the glomerulus and the odor presented. This result also
553 rules out the possibility that the differences in onset latency are an artifact caused by the measurement
554 error in inhalation onset.

555 Given that the glomerulus–odor pair was the primary determinant of onset latency, we re-examined the
556 possible contribution of cell type to the onset latency by comparing tdTomato⁺ and tdTomato⁻ cells in the
557 same glomerulus–odor pairs. We examined the relative order of onset latency within a glomerulus–odor
558 pair (see Materials and Methods) and did not see a difference with regard to tdTomato expression ($P =$
559 0.39 , $N = 41$ tdTomato⁺ and 26 tdTomato⁻ cell–odor pairs: Mann-Whitney U-test).

560 **Onset latencies of JG cells with the same odor-response profile**

561 To gain insight into the possible role of glomerular circuits in onset latency, we next compared the
562 onset latency among cells within the same glomerulus–odor pair (Fig. 7). The first observation that drew
563 our attention was that the trial-by-trial deviation of each cell (summarized as the IQR) was larger than the
564 deviation of median onset latencies across cells (Figs. 6 and 7A1–2). To understand the origin of this
565 deviation, we re-organized the data and sorted them by trial (Fig. 7A3–4). We found that the deviation of
566 onset latencies within a trial (across cells) is much smaller than the deviation within a cell (across
567 repetitions). In other words, the onset latencies were more deviated across trials (gray box-whisker plots

568 in Fig. 7A3–4) than across cells (black box-whisker plots in 7A1–2), suggesting that the large *intracell*
569 deviations are explained by the deviation across trials, which might be related, for example, to a
570 fluctuating state in the animal or to measurement error in the inhalation onset. Of note, we did not find a
571 clear relationship between the median onset latency within the trial and the order of acquisition (data not
572 shown). As presented in Fig. 7C, the IQR across trials was larger than the IQR across cells for most of the
573 glomerulus–odor pairs ($P = 2.2 \times 10^{-4}$, $N = 20$: Wilcoxon’s signed-rank test). Therefore, when the onset
574 latencies were aligned to the median of the corresponding trial, the deviation of each cell across trials
575 substantially decreased (Fig. 7B). In the case presented in Fig. 7B, the order of the aligned onset latencies
576 was well preserved between the two stimuli (note that the same color represents the same cell). Although
577 this may imply the presence of a systematic difference in onset latency among these cells, examining this
578 further would require a larger data set than we currently have, with multiple stimuli and more cells.

579 **Distribution of the rise time in single-cycle stimulation**

580 In addition to onset latency, an odor-evoked burst of action potentials can be characterized by, for
581 example, the duration and the number of spikes. With the assumption that the duration of the rising phase
582 of a calcium transient (rise time) is closely correlated with the duration of burst activity, we analyzed the
583 rise time of odor-evoked calcium transients (Fig. 8). We defined the rise time as the duration for a
584 calcium signal to rise from 20% to 80% of the peak amplitude. Because we could not distinguish
585 individual respiration cycles in the calcium transients evoked by multi-cycle stimulation, we focused
586 primarily on data from single-cycle stimulation.

587 First, we simply looked at the distribution of rise times across odor–cell pairs (Fig. 8A). As expected,
588 the large majority (84.8%) of rise times for single-cycle stimulation (blue) were shorter than 300 ms,
589 suggesting that the action potentials halted (or greatly decreased) within a single respiration cycle (300–
590 500 ms). The presence of relatively short rise times may indicate spike activity of shorter duration in these
591 cells. A minor proportion had longer rise times, likely reflecting the persistence of activity even after the
592 stimulus offset. By contrast, the rise times under 2 s stimulation (gray) were distributed more broadly,

593 reflecting the heterogeneous time courses of calcium transients in this condition (Fig. 3A). Of note, as
594 populations, rise time was not different between tdTomato⁺ and tdTomato⁻ neurons with both single-cycle
595 stimulation (tdTomato⁺: median 182 ms, N = 108 cell-odor pairs; tdTomato⁻: median 165 ms, N = 47
596 pairs; P = 0.25, Mann-Whitney U-test) and 2 s stimulation (tdTomato⁺: median 701 ms, N = 213 cell-
597 odor pairs; tdTomato⁻: median 596 ms, N = 88 pairs; P = 0.093). Next, as for onset latency (Fig. 6), we
598 grouped the data from cell-odor pairs putatively associated with the same glomerulus, to examine the
599 contribution of glomerular inputs (Fig. 8B). With single-cycle stimulation, rise times depended on the
600 glomerulus-odor pair with statistical significance ($P = 1.2 \times 10^{-6}$, 17 glomerulus-odor pairs, Kruskal-
601 Wallis test for non-uniform distribution). This was not the case for the multi-cycle stimulation ($P = 0.087$).
602 In Fig. 8B, the IQRs for each cell-odor pair (horizontal bars) were not very different from the deviation
603 among median rise times within the same group. This was in clear contrast with the results for onset
604 latency (Figs. 6 and 7A) and suggests little trial-by-trial deviation (see above).

605 As for onset latency, above, we compared the relative rise times of tdTomato⁺ and tdTomato⁻ neurons
606 putatively associated with the same glomerulus and did not see any statistically significant differences (P
607 = 0.28 for single-cycle stimulation, $P = 0.39$ for multi-cycle stimulation, N = 30 tdTomato⁺ and 14
608 tdTomato⁻ cell-odor pairs from eight glomerulus-odor pairs that included four or more neurons: Mann-
609 Whitney U-test). Finally, we examined the correlation between transient rise times and peak amplitudes,
610 as a strong correlation between these would not be compatible with our assumption that rise time reflects
611 the duration of burst activity. We only considered data from single-cycle stimulation in this analysis.
612 Since we cannot compare response amplitudes across different cells, we analyzed cells that were activated
613 by more than one odorant. For each cell, all rise times and response amplitudes were normalized to those
614 of the response with the largest peak amplitude (the reference response), and plotted in Fig. 8C (reference
615 responses are omitted but would appear at [0, 1] on the plot). Among 77 cell-odor pairs, the rise time was
616 shorter in 34 cell-odor pairs and longer in 43 cell-odor pairs than the corresponding reference response.
617 Thus, it is highly unlikely that rise time is accounted for solely by the response amplitude, which favors

618 our assumption that rise time is correlated with the duration of burst activity. When we considered
619 tdTomato⁺ and tdTomato⁻ cells separately, both cell populations have relative rise time shorter than and
620 longer than the reference response (tdTomato⁺: 23 shorter and 32 longer cell-odor pairs; tdTomato⁻: 11
621 shorter and 11 longer cell-odor pairs). And the distribution of relative rise times were overlapping
622 between tdTomato⁺ and tdTomato⁻ cells, except that the cell-odor pairs with the largest relative rise times
623 ($\log_2(\text{relative rise time}) > 1$) were mostly associated with tdTomato⁺ (Fig. 8C). This subpopulation might
624 represent a distinct subtype of PG cells.

625 Discussion

626 In this study, we recorded odor-evoked calcium transients from individual JG cells in anesthetized
627 free-breathing mice at an extremely high sampling rate and measured the onset latency and rise time of
628 the transients. We examined these properties in sets of JG cells putatively associated with the same
629 glomerulus (“homglomerular” JG cells). While the onset latency of JG cells spans ~150 ms when
630 glomerular association is not taken into account, the range of onset latencies is substantially smaller
631 (typically a few tens of milliseconds) among homglomerular JG cells. Similar glomerulus specificity
632 was also found for rise times when we presented a brief odor stimulus. These observations suggest that
633 the glomeruli (more strictly, the glomerulus-odor pairs) determine a significant portion of the response
634 time course in JG cells. *High-speed calcium recording by random-access scanning*

635 Here, we briefly discuss the technical aspects of this study. The intracellular calcium level has become
636 a popular proxy for neuronal activity (Grienberger and Konnerth, 2012). It is well acknowledged that the
637 calcium signal is much slower than the related action potentials, but this has not been a serious issue in
638 two-photon imaging studies partly owing to the low frame rates of conventional two-photon microscopes.
639 At the same time, such a situation has limited the analyses possible from readouts of the temporal patterns
640 of calcium signals *in vivo*. In this study, we used a random-access scanning technique (Iyer et al., 2006;
641 Grewe et al., 2010) and sampled the calcium transients at a high rate (667 Hz). This high sampling rate
642 was achieved by limiting the number of pixels sampled. Thus, the sampling duration *per pixel*, which

643 often limits the s/n ratio of two-photon recording, was no different from the full-frame scan. While
644 random-access scanning has tended to be utilized more for volumetric recordings of numerous cells
645 (Göbel et al., 2007; Froudarakis et al., 2014), high-fidelity recording is another powerful application of
646 the technique (Grewe et al., 2010). Technically, our scanner is capable of scanning at *per-pixel* sampling
647 rates up to ~10 times higher than in this study (with lower s/n ratio). Thus, this technique is compatible
648 with two-photon voltage recording of action potentials with voltage-sensitive fluorescence proteins,
649 which have been continuously improving in efficacy (Lin and Schnitzer, 2016; Chamberland et al., 2017).

650 *Functional feature of GAD2 positive and negative cells.*

651 Against our expectations, we did not find a clearly distinct functional difference between GAD2-
652 positive (tdTomato⁺) and GAD2-negative cells (tdTomato⁻) in this series of experiments. Although
653 tdTomato⁺ cells had a shorter onset latency than tdTomato⁻ cells in a simpler analysis (Fig. 5), our data
654 set was not sufficiently large for clarifying whether this shorter onset latency is truly associated with the
655 tdTomato expression or caused by other reasons such as uneven sampling of tdTomato⁺ and tdTomato⁻
656 cells across glomeruli. In addition, we did not see the difference in the rise time either (but see Fig. 8C).
657 We thus did not reach a firm conclusion about the difference in two populations, at the temporal
658 resolution of our methods. Of note, tdTomato⁻ cells were very likely composed of multiple cell types and
659 tdTomato⁺ cells could also include multiple subtypes of PG cells (Shao et al., 2009 ; Najac et al., 2015).
660 Heterogeneity within the tdTomato⁺ or tdTomato⁻ cells may have had a negative impact in our analyses.

661 *Heterogeneity in the dynamics of odor-evoked calcium transients*

662 In experiments with anesthetized free-breathing animals, it is common practice to present an odor
663 stimulus for several seconds, lasting over multiple respiration cycles. In our recording of odor-evoked
664 calcium transients in the GCaMP6f-expressing JG cells (dominated by PG cells), it took a different
665 number of respiration cycles to reach the transient peak in different cells (or cell-odor pairs); this is also
666 illustrated by the heterogeneity in rise times (the period from 20% to 80% of the peak signal amplitude;

667 Fig. 8A, B). It is not clear to what extent this heterogeneity is due to the spike–calcium relationship
668 (Grienberger and Konnerth, 2012) or to the temporal pattern of the spikes. The phenomenon may
669 potentially be understood better by inferring the action potentials from the calcium signals (Yaksi and
670 Friedrich, 2006; Theis et al., 2016; Rahmati et al., 2018). In this study, we did not take this path because
671 of our lack of easy means to validate the inference. It is indeed an interesting question whether such
672 methods could successfully reconstruct the action potentials in this case: reconstruction may be
673 challenging in PG cells owing to the respiration-coupled bursting activity that may make the spike–
674 calcium relationship strongly non-linear.

675 Such heterogeneous time courses also raise a practical problem for quantifying the amplitude of
676 calcium transients. For example, peak amplitude is often used to quantify the amplitude of transients, but
677 it may be associated with different numbers of respiration cycles across cells. Note that this issue is also
678 relevant to the analysis of rise time. In this study, we used single-respiration-cycle stimuli to prevent
679 signals from accumulating over multiple respiration cycles for analyses involving comparisons of the
680 response amplitude (Figs. 3 and 8C). Although we do not have enough data to address whether the
681 problem is also relevant to other types of neurons in the olfactory system, diverse calcium-transient time
682 courses have been reported in multiple cell types (Wachowiak et al., 2013). Thus, there may be other
683 cases where the shape of the calcium transients deserves consideration during the quantification of
684 response properties.

685 *Glomerular circuits and glomerulus-specific onset latency*

686 The glomerulus-specific onset latencies of JG cells are characterized by relatively small deviations in
687 onset latency within the same glomerulus and larger deviations across glomeruli. The most plausible
688 explanation for this is that the JG cells follow the onset of sensory inputs in each glomerulus, as the onset
689 latency of sensory inputs from OSNs is heterogeneous across glomeruli (Spors et al., 2006; Carey et al.,
690 2009). On the other hand, the small deviations within a glomerulus may imply that the sensory inputs
691 from many OSNs are accumulated in such a time window, given that an axon from each OSN covers a

692 small fraction of a glomerulus (Hálasz and Greer, 1993). It may then be reasonable that the recorded JG
693 cells, regardless of tdTomato expression, are activated within a time window of ~20 ms (Fig. 7), because
694 most (if not all) JG cells receive the inputs from OSNs directly or disynaptically via the local neurons
695 (Wachowiak and Shipley, 2006; Tavakoli et al., 2018). As discussed above, tdTomato⁺ and tdTomato⁻
696 cells would be driven either in parallel or with a finer difference than what was considered in this study.
697 In either case, such a temporally confined activity of excitatory and inhibitory neurons could play
698 important roles in relaying the dynamic inputs from the OSNs to the principal neurons. It is worth noting
699 that most of our analyses were limited to relatively strong responses as we only used data with a high s/n
700 ratio. It is thus an interesting question whether a weaker stimulus would broaden the distribution of onset
701 latencies among homoglomerular JG cells. If this was indeed the case, such a mechanism could play an
702 important role in the intraglomerular circuit, where many JG cells of the same type (or subtype) receive
703 homogeneous inputs and perform the same function (e.g., feedforward excitation/inhibition). For instance,
704 even if a class of JG cells collectively releases the same total amount of neurotransmitter to the
705 glomerular circuit, the consequences would be different if highly synchronized neurons release the
706 transmitter at a high density over a short time window, versus if less-synchronized neurons release the
707 transmitter at a lower density over a longer time window. We suggest such a mechanism may be useful to
708 enhance the s/n ratio of sensory inputs to the glomerulus while maintaining their dynamics.

709 *Implications for the function of the OB and glomeruli*

710 Although our recordings were limited to JG cells, the glomerulus-specific response time course of
711 these cells suggests that the time course of sensory inputs is highly glomerulus-specific. Each glomerulus
712 was driven at a different time, with a strong input in the first tens of milliseconds. The temporal pattern of
713 odor-evoked activity has been shown to be a part of stimulus representation in the principal neurons (Cury
714 and Uchida, 2010; Uchida et al., 2014). Our results support the idea that sensory inputs play a role in the
715 temporal coding of odor stimuli (Schaefer and Margrie, 2007; Raman et al., 2010). For example, a coarse
716 temporal pattern may be determined by the sensory inputs (as well as the glomerular circuits) and be

717 largely homogeneous among homoglomerular mitral cells. The odor-evoked activity, including the
718 temporal pattern, may then be refined in subsequent OB circuits so that it is diversified among individual
719 principal neurons (Dhawale et al., 2010; Kikuta et al., 2013; Arneodo et al., 2018). Furthermore,
720 glomerulus-specific onset latencies may play a role in the horizontal connections among glomeruli
721 (Aungst et al., 2003; Kiyokage et al., 2010; Banerjee et al., 2015). Early responding glomeruli may be
722 capable of modulating the activity in neighboring glomeruli more strongly, although the computational
723 advantage of such a mechanism is not obvious in a system that supposedly lacks a topographic
724 representation of stimulus space (Cleland and Sethupathy, 2006; Cleland, 2014). Similarly, lateral
725 interactions between mitral/tufted cells may also be orchestrated by the differences in their onset latencies
726 (Arneodo et al., 2018). At last, if these mechanisms make the onset latency (and maybe the duration) of
727 outputs from individual glomeruli more distinct, it would benefit the lateral interaction in the OB circuits
728 as well as the integration of signals in the olfactory centers by limiting the number of glomeruli that can
729 send the coincident inputs to the downstream neurons in a given moment.

730

731

732 **References**

- 733 Adam Y, Livneh Y, Miyamichi K, Groysman M, Luo L, Mizrahi A (2014) Functional transformations of
734 odor inputs in the mouse olfactory bulb. *Front Neural Circuits* 8:129.
- 735 Arneodo EM, Penikis KB, Rabinowitz N, Licata A, Cichy A, Zhang J, Bozza T, Rinberg D (2018)
736 Stimulus dependent diversity and stereotypy in the output of an olfactory functional unit. *Nat*
737 *Commun* 9:1347.
- 738 Aungst JL, Heyward PM, Puche AC, Karnup S V, Hayar A, Szabo G, Shipley MT (2003) Centre-
739 surround inhibition among olfactory bulb glomeruli. *Nature* 426:623–629.
- 740 Banerjee A, Marbach F, Anselmi F, Koh MS, Davis MB, Garcia da Silva P, Delevich K, Oyibo HK,
741 Gupta P, Li B, Albeanu DF (2015) An Interglomerular Circuit Gates Glomerular Output and
742 Implements Gain Control in the Mouse Olfactory Bulb. *Neuron* 87:193–207.
- 743 Braubach O, Tombaz T, Geiller T, Homma R, Bozza T, Cohen LB, Choi Y (2018) Sparsened neuronal
744 activity in an optogenetically activated olfactory glomerulus. *Sci Rep* 8:14955.
- 745 Burton SD (2017) Inhibitory circuits of the mammalian main olfactory bulb. *J Neurophysiol* 118:2034–
746 2051.
- 747 Carey RM, Sherwood WE, Shipley MT, Borisyyuk A, Wachowiak M (2015) Role of intraglomerular
748 circuits in shaping temporally structured responses to naturalistic inhalation-driven sensory input to
749 the olfactory bulb. *J Neurophysiol* 113:3112–3129.
- 750 Carey RM, Verhagen J V, Wesson DW, Pérez N, Wachowiak M (2009) Temporal structure of receptor
751 neuron input to the olfactory bulb imaged in behaving rats. *J Neurophysiol* 101:1073–1088.
- 752 Chamberland S, Yang HH, Pan MM, Evans SW, Guan S, Chavarha M, Yang Y, Salesse C, Wu H, Wu JC,
753 Clandinin TR, Toth K, Lin MZ, St-Pierre F (2017) Fast two-photon imaging of subcellular voltage
754 dynamics in neuronal tissue with genetically encoded indicators. *Elife* 6:e25690.

- 755 Chen TW, Wardill TJ, Sun Y, Pulver SR, Renninger SL, Baohan A, Schreiter ER, Kerr RA, Orger MB,
756 Jayaraman V, Looger LL, Svoboda K, Kim DS (2013) Ultrasensitive fluorescent proteins for imaging
757 neuronal activity. *Nature* 499:295–300.
- 758 Cleland TA (2014) Construction of odor representations by olfactory bulb microcircuits. *Prog Brain Res*
759 208:177–203.
- 760 Cleland T, Sethupathy P (2006) Non-topographical contrast enhancement in the olfactory bulb. *BMC*
761 *Neurosci* 7:7.
- 762 Cury KM, Uchida N (2010) Robust odor coding via inhalation-coupled transient activity in the
763 mammalian olfactory bulb. *Neuron* 68:570–585.
- 764 De Saint Jan D, Hirnet D, Westbrook GL, Charpak S (2009) External tufted cells drive the output of
765 olfactory bulb glomeruli. *J Neurosci* 29:2043–2052.
- 766 Dhawale AK, Hagiwara A, Bhalla US, Murthy VN, Albeanu DF (2010) Non-redundant odor coding by
767 sister mitral cells revealed by light addressable glomeruli in the mouse. *Nat Neurosci* 13:1404–1412.
- 768 Froudarakis E, Berens P, Ecker AS, Cotton RJ, Sinz FH, Yatsenko D, Saggau P, Bethge M, Tolias AS
769 (2014) Population code in mouse V1 facilitates readout of natural scenes through increased
770 sparseness. *Nat Neurosci* 17:851–857.
- 771 Fukunaga I, Herb JT, Kollo M, Boyden ES, Schaefer AT (2014) Independent control of gamma and theta
772 activity by distinct interneuron networks in the olfactory bulb. *Nat Neurosci* 17:1208–1216.
- 773 Geramita M, Urban NN (2017) Differences in Glomerular-Layer-Mediated Feedforward Inhibition onto
774 Mitral and Tufted Cells Lead to Distinct Modes of Intensity Coding. *J Neurosci* 37:1428–1438.
- 775 Göbel W, Kampa BM, Helmchen F (2007) Imaging cellular network dynamics in three dimensions using
776 fast 3D laser scanning. *Nat Methods* 4:73–79.

- 777 Grewe BF, Langer D, Kasper H, Kampa BM, Helmchen F (2010) High-speed in vivo calcium imaging
778 reveals neuronal network activity with near-millisecond precision. *Nat Methods* 7:399–405.
- 779 Grienberger C, Konnerth A (2012) Imaging Calcium in Neurons. *Neuron* 73:862–885.
- 780 Grimaud J, Murthy VN (2018) How to monitor breathing in laboratory rodents: a review of the current
781 methods. *J Neurophysiol* 120:624–632.
- 782 Hálasz N, Greer CA (1993) Terminal arborizations of olfactory nerve fibers in the glomeruli of the
783 olfactory bulb. *J Comp Neurol* 337:307–316.
- 784 Hayar A, Karnup S, Shipley MT, Ennis M (2004) Olfactory bulb glomeruli: external tufted cells
785 intrinsically burst at theta frequency and are entrained by patterned olfactory input. *J Neurosci*
786 24:1190–1199.
- 787 Homma R, Kovalchuk Y, Konnerth A, Cohen LB, Garaschuk O (2013) In vivo functional properties of
788 juxtglomerular neurons in the mouse olfactory bulb. *Front Neural Circuits* 7:23.
- 789 Iyer V, Hoogland TM, Saggau P (2006) Fast functional imaging of single neurons using random-access
790 multiphoton (RAMP) microscopy. *J Neurophysiol* 95:535–545.
- 791 Kikuta S, Fletcher ML, Homma R, Yamasoba T, Nagayama S (2013) Odorant Response Properties of
792 Individual Neurons in an Olfactory Glomerular Module. *Neuron* 77:1122–1135.
- 793 Kiyokage E, Pan Y-Z, Shao Z, Kobayashi K, Szabo G, Yanagawa Y, Obata K, Okano H, Toida K, Puche
794 AC, Shipley MT (2010) Molecular identity of periglomerular and short axon cells. *J Neurosci*
795 30:1185–1196.
- 796 Kosaka T, Kosaka K (2014) Olfactory Bulb Anatomy. *Ref Modul Biomed Sci* doi:10.1016/B978-0-12-
797 801238-3.04705-X.

- 798 Kosaka T, Kosaka K (2016) Neuronal organization of the main olfactory bulb revisited. *Anat Sci Int*
799 91:115–127.
- 800 Lin MZ, Schnitzer MJ (2016) Genetically encoded indicators of neuronal activity. *Nat Neurosci* 19:1142–
801 1153.
- 802 Livneh Y, Adam Y, Mizrahi A (2014) Odor Processing by Adult-Born Neurons. *Neuron* 81:1097–1110.
- 803 Lv X, Zhan C, Zeng S, Chen WR, Luo Q (2006) Construction of multiphoton laser scanning microscope
804 based on dual-axis acousto-optic deflector. *Rev Sci Instrum* 77:046101.
- 805 Macrides F, Schneider SP (1982) Laminar organization of mitral and tufted cells in the main olfactory
806 bulb of the adult hamster. *J Comp Neurol* 208:419–430.
- 807 Madisen L, Zwingman TA, Sunkin SM, Oh SW, Zariwala HA, Gu H, Ng LL, Palmiter RD, Hawrylycz
808 MJ, Jones AR, Lein ES, Zeng H (2010) A robust and high-throughput Cre reporting and
809 characterization system for the whole mouse brain. *Nat Neurosci* 13:133–140.
- 810 Mori K, Takahashi YK, Igarashi KM, Yamaguchi M (2006) Maps of Odorant Molecular Features in the
811 Mammalian Olfactory Bulb. *Physiol Rev* 86:409–433.
- 812 Nagayama S, Homma R, Imamura F (2014) Neuronal organization of olfactory bulb circuits. *Front*
813 *Neural Circuits* 8:98.
- 814 Najac M, De Saint Jan D, Reguero L, Grandes P, Charpak S (2011) Monosynaptic and polysynaptic feed-
815 forward inputs to mitral cells from olfactory sensory neurons. *J Neurosci* 31:8722–8729.
- 816 Najac M, Sanz Diez A, Kumar A, Benito N, Charpak S, De Saint Jan D (2015) Intraglomerular Lateral
817 Inhibition Promotes Spike Timing Variability in Principal Neurons of the Olfactory Bulb. *J Neurosci*
818 35:4319–4331.

- 819 Parrish-Aungst S, Shipley MT, Erdelyi F, Szabo G, Puche AC (2007) Quantitative analysis of neuronal
820 diversity in the mouse olfactory bulb. *J Comp Neurol* 501:825–836.
- 821 Pinching AJ, Powell TP (1971) The neuron types of the glomerular layer of the olfactory bulb. *J Cell Sci*
822 9:305–345.
- 823 Rahmati V, Kirmse K, Holthoff K, Kiebel SJ (2018) Ultra-fast accurate reconstruction of spiking activity
824 from calcium imaging data. *J Neurophysiol* 119:1863–1878.
- 825 Raman B, Joseph J, Tang J, Stopfer M (2010) Temporally diverse firing patterns in olfactory receptor
826 neurons underlie spatiotemporal neural codes for odors. *J Neurosci* 30:1994–2006.
- 827 Schaefer AT, Margrie TW (2007) Spatiotemporal representations in the olfactory system. *Trends*
828 *Neurosci* 30:92–100.
- 829 Schindelin J, Arganda-Carreras I, Frise E, Kaynig V, Longair M, Pietzsch T, Preibisch S, Rueden C,
830 Saalfeld S, Schmid B, Tinevez J-Y, White DJ, Hartenstein V, Eliceiri K, Tomancak P, Cardona A
831 (2012) Fiji: an open-source platform for biological-image analysis. *Nat Methods* 9:676–682.
- 832 Shao Z, Puche AC, Kiyokage E, Szabo G, Shipley MT (2009) Two GABAergic intraglomerular circuits
833 differentially regulate tonic and phasic presynaptic inhibition of olfactory nerve terminals. *J*
834 *Neurophysiol* 101:1988–2001.
- 835 Shao Z, Puche AC, Liu S, Shipley MT (2012) Intraglomerular inhibition Shapes the Strength and
836 Temporal Structure of Glomerular Output. *J Neurophysiol* 108:782–793.
- 837 Spors H, Wachowiak M, Cohen LB, Friedrich RW (2006) Temporal dynamics and latency patterns of
838 receptor neuron input to the olfactory bulb. *J Neurosci* 26:1247–1259.
- 839 Tan J, Savigner A, Ma M, Luo M (2010) Odor information processing by the olfactory bulb analyzed in
840 gene-targeted mice. *Neuron* 65:912–926.

- 841 Taniguchi H, He M, Wu P, Kim S, Paik R, Sugino K, Kvitsani D, Fu Y, Lu J, Lin Y, Miyoshi G, Shima Y,
842 Fishell G, Nelson SB, Huang ZJ (2011) A Resource of Cre Driver Lines for Genetic Targeting of
843 GABAergic Neurons in Cerebral Cortex. *Neuron* 71:995–1013.
- 844 Tavakoli A, Schmaltz A, Schwarz D, Margrie TW, Schaefer AT, Kollo M (2018) Quantitative
845 Association of Anatomical and Functional Classes of Olfactory Bulb Neurons. *J Neurosci* 38:7204–
846 7220.
- 847 Theis L, Berens P, Froudarakis E, Reimer J, Román Rosón M, Baden T, Euler T, Tolias AS, Bethge M
848 (2016) Benchmarking Spike Rate Inference in Population Calcium Imaging. *Neuron* 90:471–482.
- 849 Uchida N, Poo C, Haddad R (2014) Coding and Transformations in the Olfactory System. *Annu Rev*
850 *Neurosci* 37:363–385.
- 851 Wachowiak M, Economo MN, Diaz-Quesada M, Brunert D, Wesson DW, White JA, Rothermel M
852 (2013) Optical Dissection of Odor Information Processing In Vivo Using GCaMPs Expressed in
853 Specified Cell Types of the Olfactory Bulb. *J Neurosci* 33:5285–5300.
- 854 Wachowiak M, Shipley MT (2006) Coding and synaptic processing of sensory information in the
855 glomerular layer of the olfactory bulb. *Semin Cell Dev Biol* 17:411–423.
- 856 Wellis DP, Scott JW (1990) Intracellular responses of identified rat olfactory bulb interneurons to
857 electrical and odor stimulation. *J Neurophysiol* 64:932–947.
- 858 Yaksi E, Friedrich RW (2006) Reconstruction of firing rate changes across neuronal populations by
859 temporally deconvolved Ca²⁺ imaging. *Nat Methods* 3:377–383.
- 860

861 **Figure Legends**

862

863 Figure 1. Expression patterns of tdTomato.

864 The progeny of Gad2-IRES-Cre and cre-dependent tdTomato reporter mice were used in this study. A1–3.
865 Spatial pattern of immunolabeled GABA (A1), tdTomato (A2), and the merged image (A3). The region
866 indicated by a white box in the top panels is presented at a higher magnification in the corresponding
867 bottom panels. B1–3. Spatial pattern of immunolabeled TH (B1), tdTomato (B2), and the merged image
868 (B3). White and yellow arrowheads indicate examples of TH⁺/tdTomato⁺ cells and TH⁺/tdTomato⁻ cells,
869 respectively. Approximate positions of layer boundaries are indicated by black dotted lines in the space
870 between the panels A3 and B1. Scale bars: 50 μm.

871

872 Figure 2. Activity ($\Delta F/F_0$) maps color-coded by the phase of response in wide-field and two-photon
873 imaging.

874 A1. Surface image for wide-field (single-photon) imaging. Scale bar: 500 μm. A2–4. Maps of odor-
875 evoked response to 4CHO, 5CHO, and 6CHO, respectively. Each map is a synthesis of red, green, and
876 blue maps that represent the periods early (0.5–2.5 s), intermediate (2.5–4.5 s), and late (4.5–6.5 s)
877 periods after stimulus onset, respectively. The duration of stimulus was 2 s. This visualization allows to
878 map the heterogeneity of response time courses. For example, glomeruli that declined quickly after the
879 stimulation appear in red (e.g. lateral glomeruli in A2–4), while those with persistent response appear in
880 yellow or white as they maintained the high-level calcium over the first two or all three periods (e.g.
881 subsets of medial glomeruli in A2–4). Glomeruli that appear in bluish colors are slow-rising ones. B1. A
882 two-photon image of the selected area, indicated by the black box in A1 and by white corners in A2–4.
883 Scale bar: 50 μm. B2–4. Maps of odor-evoked response, with the colors representing the same periods as
884 in A2–4.

885

886 Figure 3. Odor-evoked calcium transients and grouping of JG cells by response profile.

887 A. An example data set from a single trial of random-access scanning of 15 ROIs (cells). Left traces are
888 responses to a 2 s odor stimulus, and right traces are responses to a single-respiration-cycle stimulus. The
889 bottom black traces show the respiration signal. Gray horizontal bars above the respiration signals
890 indicate the timing of valve opening for odor presentation. Note that actual odor presentation lags
891 approximately 0.1 s behind the valve opening. The ordering of the ROIs is intentional, based on the result
892 of grouping shown in C. B. Two-photon image of the recording site (B1) and the ROI indexes (B2). To
893 obtain the two-photon image of GCaMP6f (green), all XYT imaging data for all odors were averaged and
894 then all post-stimulus frames were averaged, solely for making the GCaMP fluorescence more visible.
895 The tdTomato image (magenta) were obtained with a similar procedure, but an average of pre-stimulus
896 frames were used. Dots and contours represent the ROIs and glomeruli, respectively. Non-white colors of
897 dots and contours in B2 indicate the groups presented in C. Scale bar: 50 μm . C. Odor-evoked responses
898 of the same ROIs to five odors (single-cycle stimulus). The left block shows the response time courses.
899 The middle block shows the areas under the time courses as bar charts. The right block shows the
900 difference in areas between every possible pair of odors. Colored vertical lines at the right indicate the
901 groups of cells putatively associated with the same glomerulus (see text for details). Scale bars: 3 s
902 (horizontal), 100% $\Delta F/F_0$ (vertical).

903

904 Figure 4. Characterization of calcium signals in the pre-stimulus period.

905 A. An example data of the pre-stimulus period and the initial part of odor-evoked response in a trial.
906 Green traces are the signal from the green channel (GCaMP6f), and magenta traces are the signal from the
907 red channel (tdTomato). Apparent odor-evoked changes in some of the magenta traces (e.g., ROI 10)
908 suggest a minor contribution of the GCaMP signal to the red channel. The relative contribution from the

909 GCaMP signal may vary depending on the relative expression levels of GCaMP and tdTomato at an
910 individual ROI. Note clear respiration-coupled modulations of the odor-evoked response in the subset of
911 traces. B. Two-photon image of the recording site. The image was obtained with the same procedure for
912 the image in Fig. 3B1. ROIs were indicated by white dots and the index of each dot is shown on the right
913 of image. Scale bar: 50 μm . C. Stacked histogram of the ratio between peak response amplitude and range
914 (the distance between the 1st and 99th percentiles) in the pre-stimulus period. Note the logarithmic scale
915 on the x-axis. The response is much larger than the fluctuations in the pre-stimulus period in the vast
916 majority of cases. D. Histograms showing the distribution of pairwise correlation coefficients for the time
917 courses of activity during the pre-stimulus period. Upper and lower histograms show data from cell pairs
918 putatively associated with the same glomerulus and pairs from different glomeruli, respectively.

919

920 Figure 5. Onset latencies of odor-evoked calcium transients are heterogeneous across JG cells.

921 A. Graphic representation of the definition of onset latency. (a) Baseline, defined as the mean of the pre-
922 stimulus period signal. (b) Threshold, defined as 2.5 times the standard deviation of the pre-stimulus
923 period signal. (c) Time point at which the signal exceeds the threshold. (d) Time window of the first 100
924 ms above the threshold. (e) Regression line of the signal in the 100 ms time window. (f) Point where the
925 regression line crosses the baseline. This time point is considered the onset of the calcium transient. (g)
926 Onset of the first inhalation with the odor stimulus. (h) Onset latency, defined as the distance between the
927 onset of inhalation and the onset of the calcium transient. B. Distribution of onset latencies. Each row
928 corresponds to a single cell-odor pair and the distribution of onset latencies across repetitions is presented
929 as a box-and-whisker plot (see inset). Dots in the box-and-whisker plots represent the median, and
930 expression of the GAD2 marker tdTomato is indicated by the dot color (red for tdTomato⁺ and black for
931 tdTomato⁻). Cell-odor pairs are arranged according to median onset latency and every other pair is
932 presented for clarity (83 cell-odor pairs from 8 recording sites, out of all 165 pairs, are presented). Each
933 box-and-whisker plot represents data from 5–17 trials. C. Overlapping histograms showing the

934 distribution of medians shown in B for tdTomato⁺ (red) and tdTomato⁻ (gray) cell populations. Triangles
935 in the top indicates median for each population (tdTomato⁺: 84 ms, 105 cell-odor pairs; tdTomato⁻: 108
936 ms, 60 cell-odor pairs; P = 0.012, Mann-Whitney U-test).

937

938 Figure 6. JG-cell onset latency strongly depends on the putative glomerular association.

939 A subset of the box-and-whisker plot from Fig. 5B is presented, rearranged according to glomerulus-odor
940 pairs. To clarify, cell-odor pairs in this figure include those not actually presented in Fig. 5B, where only
941 half of the cell-odor pairs are shown for clarity. As in Fig. 5B, each row represents a single-odor pair, in
942 which distribution of onset latency across repetitions were presented as box-and-whisker plots. Different
943 glomeruli are presented in different colors. In some of the glomeruli, data from more than one odorant
944 were available. Dots in the box-and-whisker plots represent the median, and expression of the GAD2
945 marker tdTomato is indicated by the dot color (red for tdTomato⁺ and black for tdTomato⁻). No statistical
946 difference was observed between the onset latencies of tdTomato⁺ and tdTomato⁻ cells, considering the
947 glomerulus-odor pairs (see text for detail). Mouse and glomerulus identity are at the left. Odorant is
948 indicated at the right.

949

950 Figure 7. Detailed analysis of onset latency across cells putatively associated with the same glomerulus.

951 The onset latencies of cell-odor pairs from a glomerulus in mouse 4 (see Fig. 6) are presented with an
952 alternative visualization. A1-2. Reconstruction of plots in Fig. 6, except that each trial was explicitly
953 plotted as circles. Each row represents an individual cell, as in Fig. 6. The median and inter-quartile range
954 for each cell are presented as the accompanying vertical and horizontal lines, respectively. Colors
955 represent individual cells and are preserved across all graphs in panels A and B. The cells are sorted by
956 their median onset latency. Left and right graphs show the responses to two different odors. The black
957 box-and-whisker plots at the bottom of each panel show the distribution of median onset latency across

958 cells. A3–4. The same data as in A1–2, but rearranged so that each row represents an individual trial.
959 Note that the variances within individual rows are markedly smaller than those in panels A1–2,
960 suggesting that the primary cause of *intracell* deviation in panels A1, A2 are trial-by-trial variability and
961 not random errors. Trials are sorted according to their median onset latency, not by the order of
962 acquisition. The gray box-and-whisker plots at the bottom of each panel show the distribution of median
963 onset latency across trials. B1–2. Onset latencies are plotted as in A1–2, except for that the contribution of
964 trial-by-trial variance was removed. Specifically, the median onset latency across the in-group cells in the
965 corresponding trial is subtracted from each data point. C. Inter-quartile ranges (IQRs) of median onset
966 latency across cells (black circles, corresponding to the black box-and-whisker plots in A1–2) and across
967 trials (gray circles, corresponding to the gray box-and-whisker plots in A3–4) in each glomerulus-odor
968 pairs are compared for all glomerulus-odor pairs shown in Fig. 6. IQRs across cells are smaller in nearly
969 all cases. Red triangle indicates the IQR of onset latency across all glomerulus-odor pairs involved in this
970 analysis (50 ms). (The onset latency of a glomerulus-odor pair is defined as the median of medians across
971 involved cells.) This value is much larger than IQRs across cells in each glomerulus-odor pairs (black
972 circles), but is close to the IQRs across all cell–odor pairs pooled (blue triangle, 55 ms, 88 cell–odor
973 pairs), suggesting that the spread of IQRs across all cell–odor pairs are primarily accounted for by the
974 spread across glomerulus-odor pairs.

975

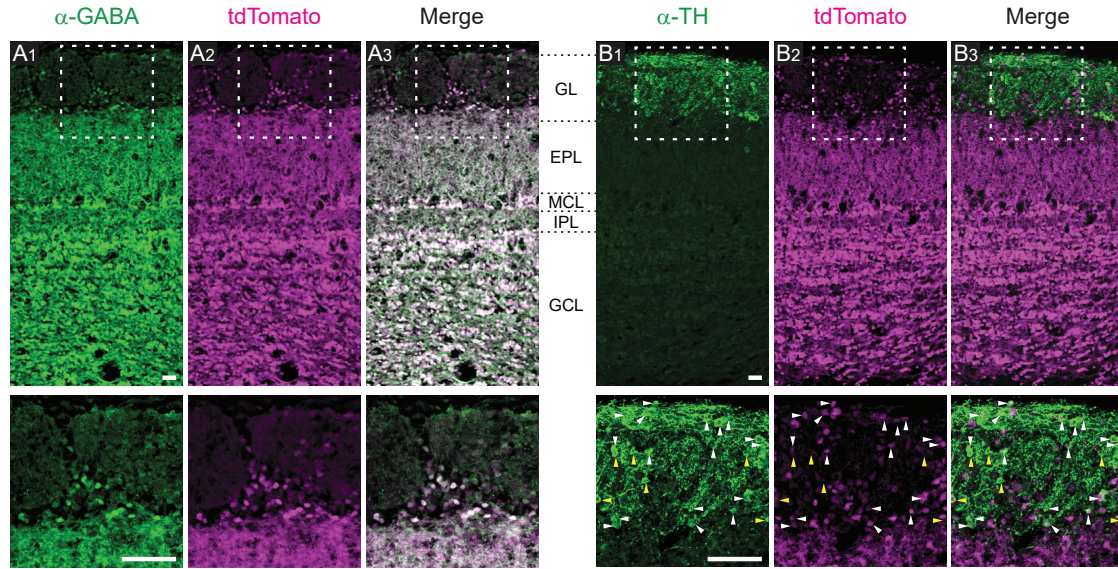
976 Figure 8. Analyses of the rise time of odor-evoked calcium transients.

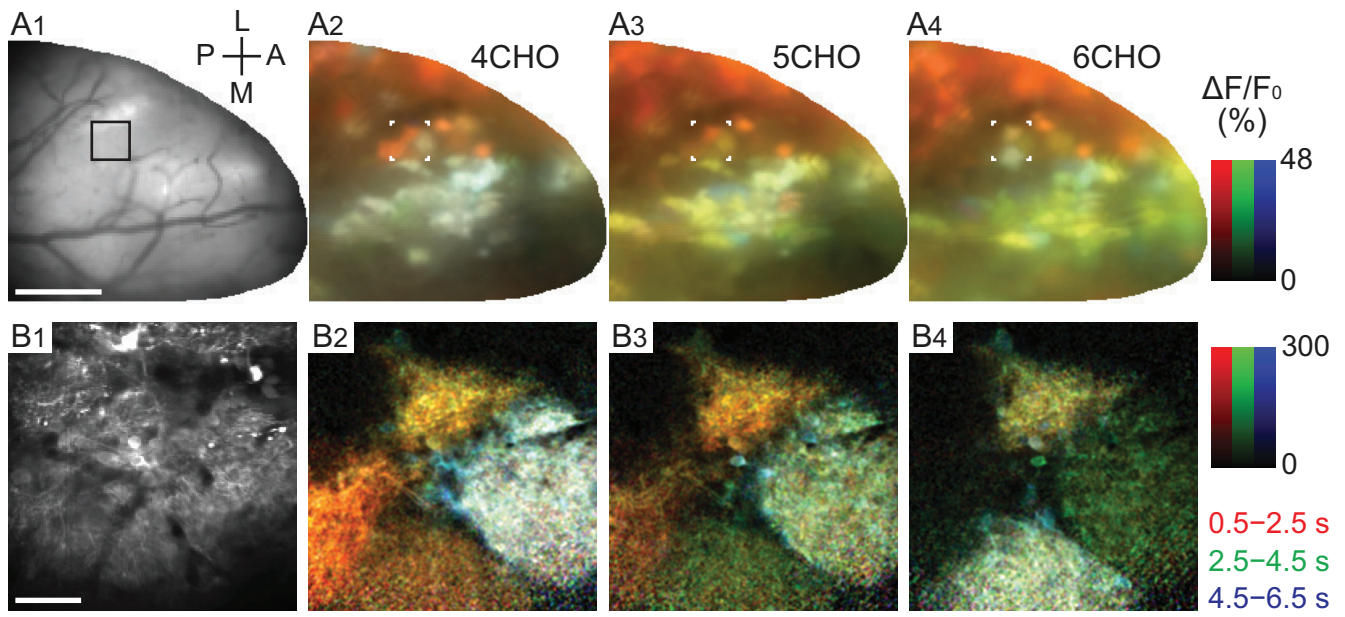
977 A. Distribution of rise times, defined as the duration between the points when a signal reached 20% and
978 80% of peak amplitude. Two overlapping histograms are presented. The blue histogram represents the
979 distribution of single-cycle stimulation, and the gray one represents the distribution of multi-cycle (2 s)
980 stimulation. B. Rise times are presented for cells putatively associated with the same glomerulus. All
981 cases in which rise time was successfully determined in three or more cells are presented. The median is
982 presented as a diamond, and the inter-quartile range as a horizontal bar. No horizontal bar means that the

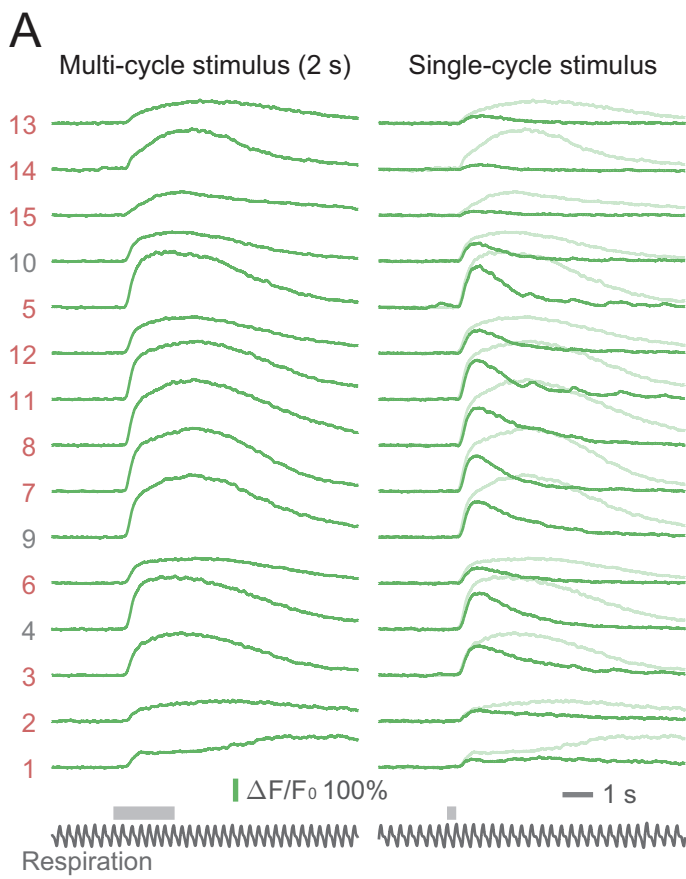
983 inter-quartile range is smaller than the size of the diamond marker. In the right panel (multi-cycle
984 stimulation), the data from the left panel (single-cycle stimulation) are replicated in gray to facilitate
985 comparison. Note the logarithmic scale on the x-axis. Expression of the GAD2 marker tdTomato (positive
986 (+) or negative (-)) is indicated at the right. The indexes for mouse and glomerulus are shown at the left:
987 these indexes correspond to those in Fig. 6. C. The relationship between onset latency and peak response
988 amplitude is plotted. Because peak amplitudes can be compared only within the same cell, only data from
989 cells in which the rise time was successfully determined for more than one odorant were used in the
990 analysis (see text for details). Red and black circles represent the data point from tdTomato⁺ and
991 tdTomato⁻ cells, respectively. The set of box-and-whisker plots in the bottom show the distribution of
992 tdTomato⁺ and tdTomato⁻ cells, in which cell-odor pairs with shorter rise time than the reference cell and
993 those with longer rise time are considered separately. The difference of distribution is statistically tested
994 for matching pairs as shown in the figure, where negative relative rise times in logarithm are converted to
995 their absolute values (tdTomato⁺: 32 cell-odor pairs with relative rise time > 1, 22 pairs with < 1;
996 tdTomato⁻: 11 cell-odor pairs with relative rise time > 1, 11 pairs with < 1, Mann-Whitney U-test). Note
997 the logarithmic scale on the x-axis.

998

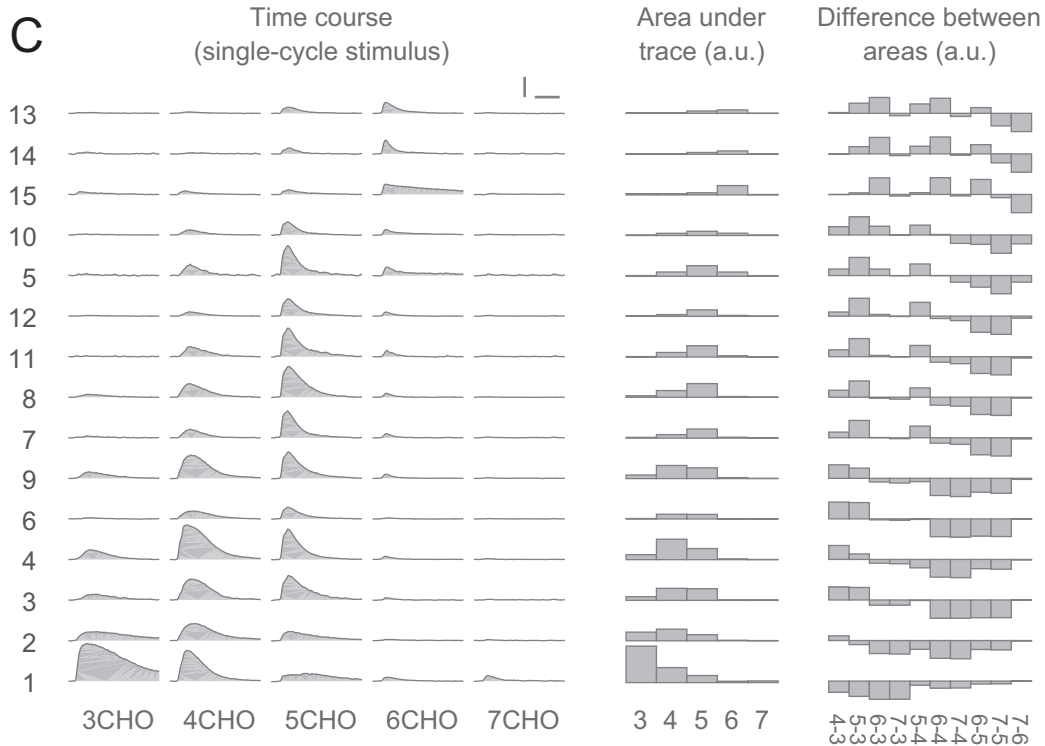
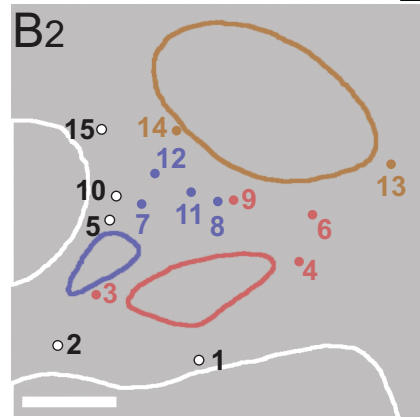
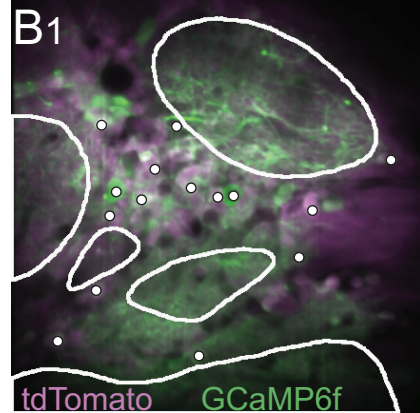
Gad2-ires-Cre x tdTomato reporter (Ai9)

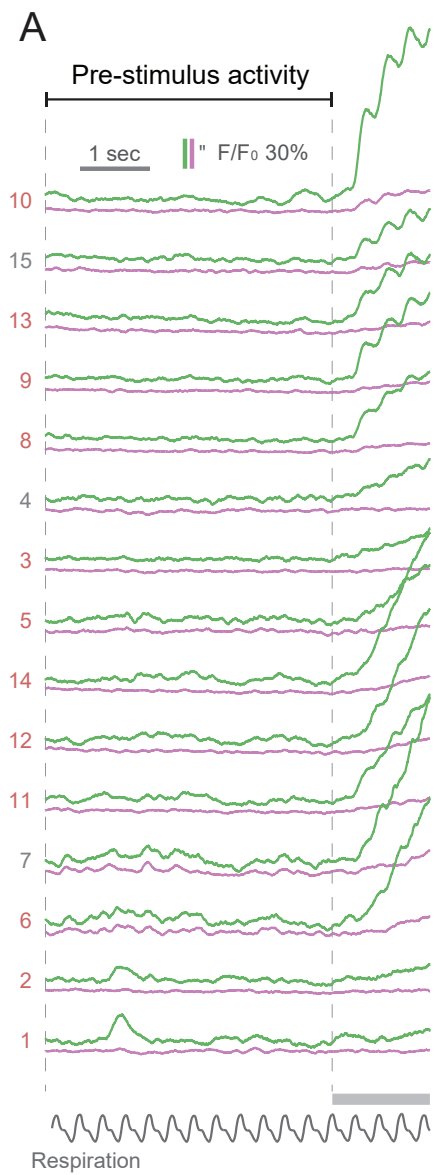




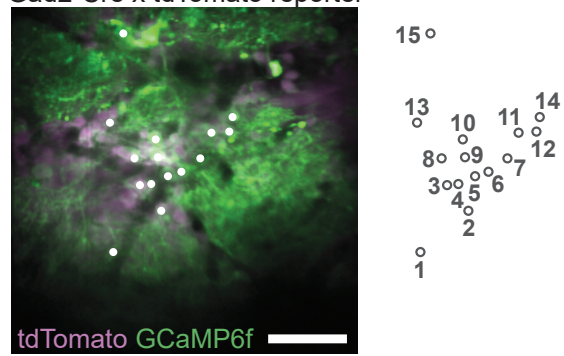


Gad2-Cre x tdTomato reporter

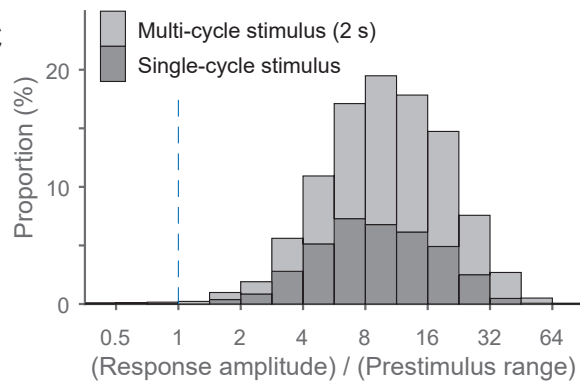




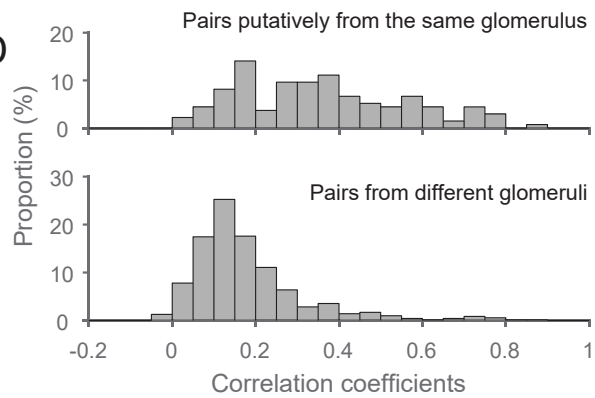
B Gad2-Cre x tdTomato reporter



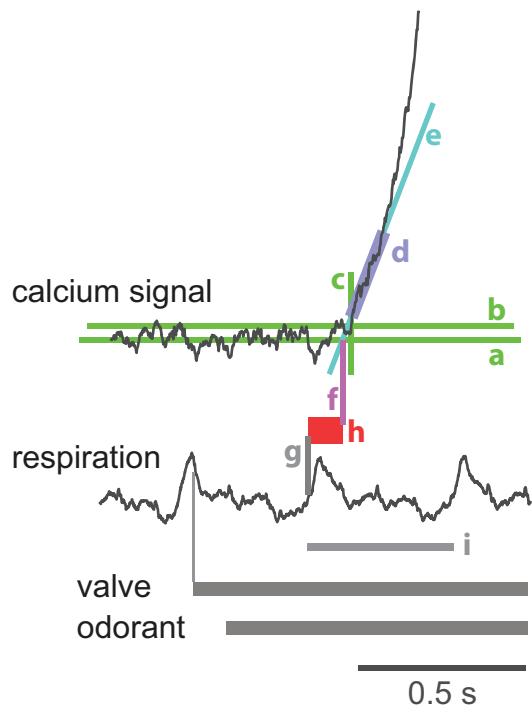
C



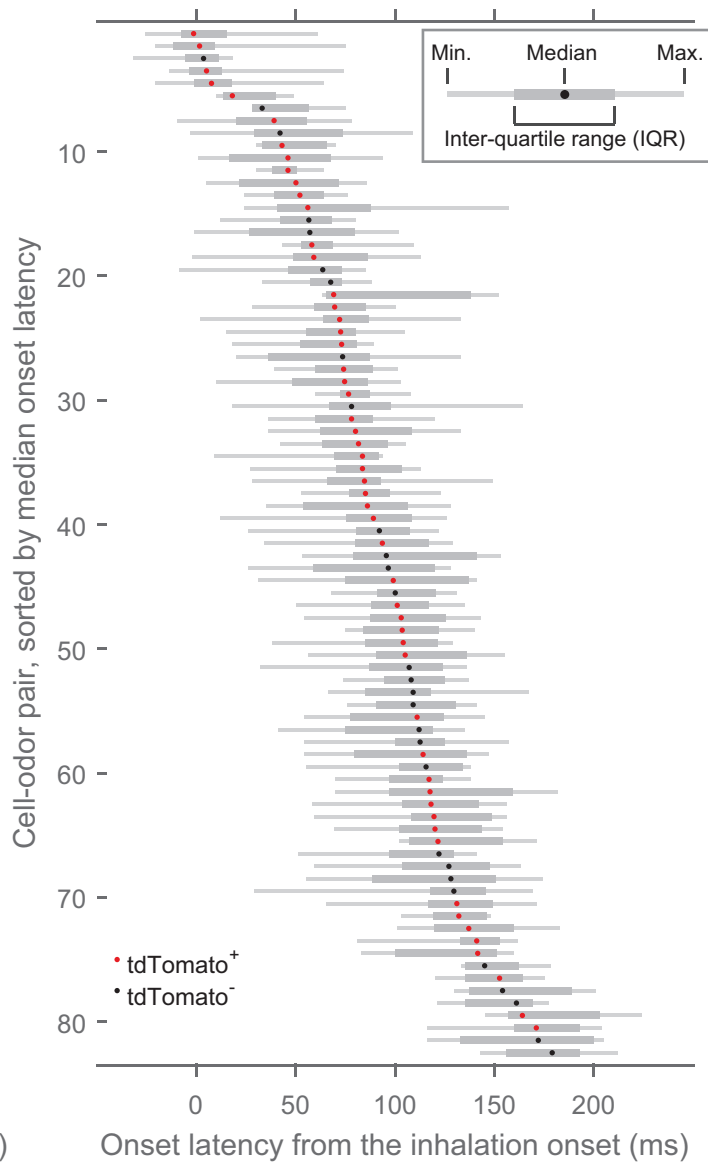
D



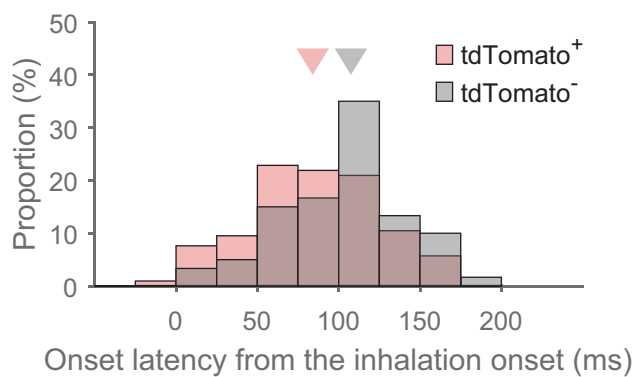
A

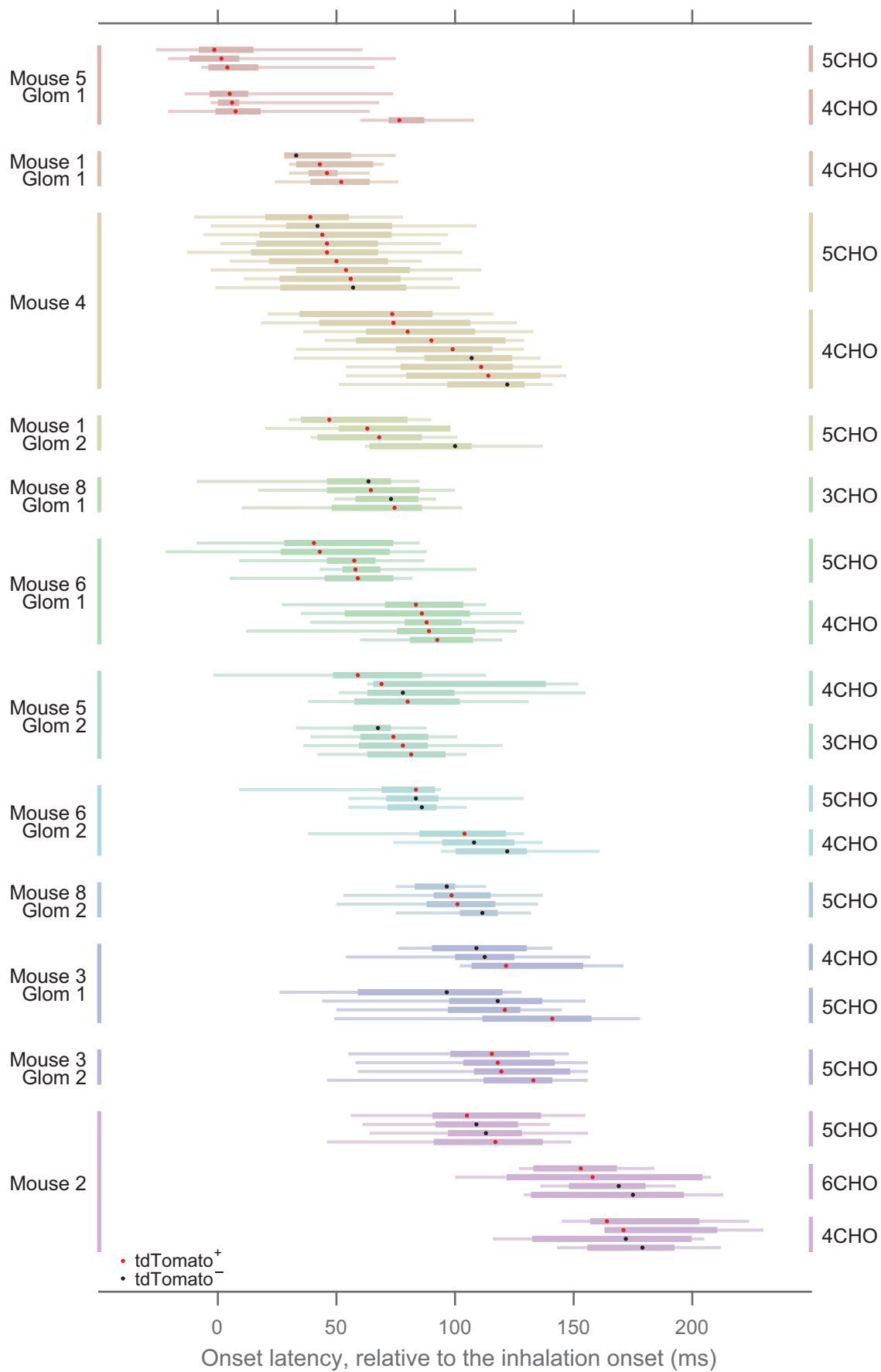


B

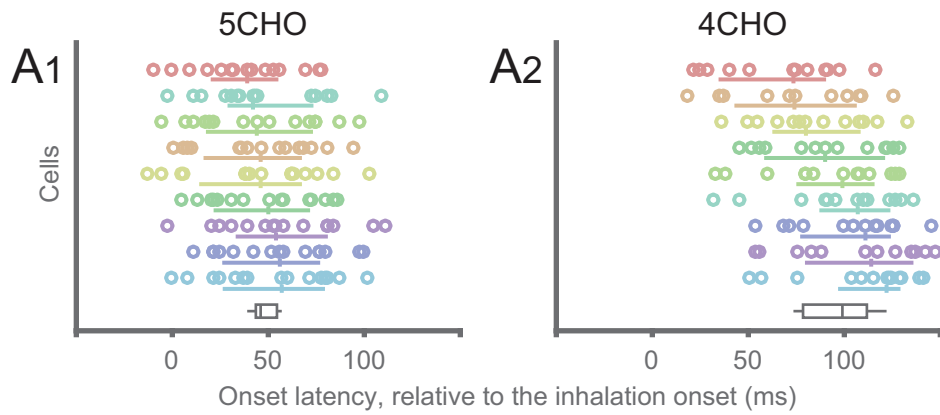


C

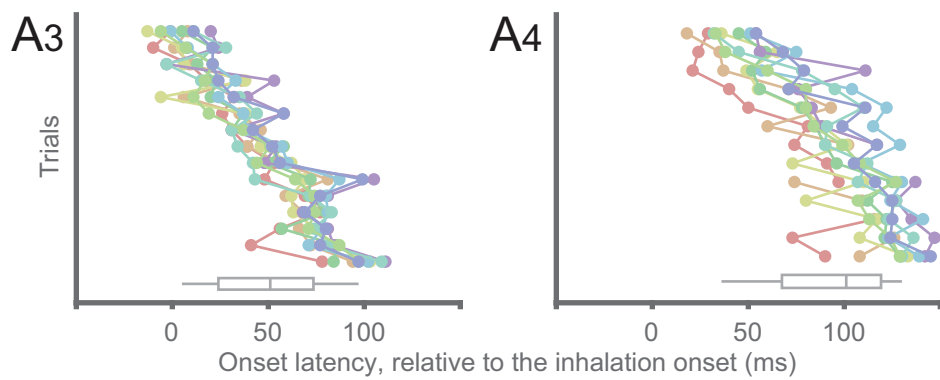




Onset latencies of 9 cells across repetitions (mouse 4)



Onset latencies of the same cells in 13 repetitions



Onset latencies, corrected for the trial-by-trial deviation

